POTENTIAL SINGULARITY OF THE AXISYMMETRIC EULER EQUATIONS WITH C^α INITIAL VORTICITY FOR A LARGE RANGE OF α. PART I: THE 3-DIMENSIONAL CASE

THOMAS Y. HOU* AND SHUMAO ZHANG†

Abstract. In Part I of our sequence of 2 papers, we provide numerical evidence for a potential finite-time self-similar singularity of the 3D axisymmetric Euler equations with no swirl and with C^α initial vorticity for a large range of α. We employ an adaptive mesh method using a highly effective mesh to resolve the potential singularity sufficiently close to the potential blow-up time. Resolution study shows that our numerical method is at least second-order accurate. Scaling analysis and the dynamic rescaling formulation are presented to quantitatively study the scaling properties of the potential singularity. We demonstrate that this potential blow-up is stable with respect to the perturbation of initial data. Our study shows that the 3D Euler equations with our initial data develop finite-time blow-up when the Hölder exponent α is smaller than some critical value α^*. By properly rescaling the initial data in the z-axis, this upper bound for potential blow-up α^* can asymptotically approach 1/3. Compared with Elgindi's blow-up result in a similar setting [15], our potential blow-up scenario has a different Hölder continuity property in the initial data and the scaling properties of the two initial data are also quite different.

Key words. 3D axisymmetric Euler equations, finite-time blow-up

AMS subject classifications. 35Q31, 76B03, 65M60, 65M06, 65M20

1. Introduction. The three-dimensional (3D) incompressible Euler equations in fluid dynamics describe the motion of inviscid incompressible flows and are one of the most fundamental equations in fluid dynamics. Despite their wide range of applications, the question regarding the global regularity of the Euler equations has been widely recognized as a major open problem in partial differential equations (PDEs) and is closely related to the Millennium Prize Problem on the Navier-Stokes equations listed by the Clay Mathematics Institute [16]. In 2014, Luo and Hou [35, 36] considered the 3D axisyemmtric Euler equations with smooth initial data and boundary, and presented strong numerical evidences that they can develop potential finite time singularity. The presence of the boundary, the symmetry properties and the direction of the flow in the initial data collaborate with each other in the formation of a sustainable finite time singularity. Recently, Chen and Hou [6] provided a rigorous justification of the Luo-Hou blow-up scenario.

In 2021, Elgindi [15] showed that given appropriate C^α initial vorticity with $\alpha > 0$ sufficiently small, the 3D axisymmetric Euler equations with no swirl can develop finite-time singularity. In Elgindi's work, the initial data for the vorticity ω have C^α Hölder continuity near $r = 0$ and $z = 0$. When α is small enough, Elgindi approximated the 3D axisymmetric Euler equations by a fundamental model that develops a self-similar finite-time singularity. The blow-up result obtained in [15] has infinite energy. In a subsequent paper [13], the authors improved the result obtained in [15] to have finite energy blow-up.

In this work we study potential finite time singularity of the 3D axisymmetric Euler equations with no swirl and C^α initial vorticity for a large range of α. Define $\omega = \nabla \times u$ as the vorticity vector, and then the 3D incompressible Euler equations

*Department of Computing and Mathematical Sciences, California Institute of Technology, Pasadena, CA (hou@cms.caltech.edu).

†Department of Computing and Mathematical Sciences, California Institute of Technology, Pasadena, CA (shumaoz@caltech.edu).

can be written in the vorticity stream function formulation:

$$\begin{aligned} \omega_t + u \cdot \nabla \omega &= \omega \cdot \nabla u, \\ -\nabla \psi &= \omega, \\ u &= \nabla \times \psi, \end{aligned} \tag{1.1}$$

where ψ is the vector-valued stream function. Let us use $x = (x_1, x_2, x_3)$ to denote a point in $\mathbb{R}^3$, and let e_r, e_θ, e_z be the unit vectors of the cylindrical coordinate system

$$e_r = \frac{1}{r}\left(x_1, x_2, 0\right), \quad e_\theta = \frac{1}{r}\left(x_2, -x_1, 0\right), \quad e_z = \left(0, 0, 1\right),$$

where $r = \sqrt{x_1^2 + x_2^2}$ and $z = x_3$. We say a vector field v is axisymmetric if it admits the decomposition

$$v = v^r(r,z)e_r + v^\theta(r,z)e_\theta + v^z(r,z)e_z,$$

namely, v^r, v^θ and v^z are independent of the angular variable θ. Denote by u^θ, ω^θ, and ψ^θ the angular velocity, vorticity and stream function, respectively. The axisymmetric condition can then simplify the 3D Euler equations (1.1) to [38]:

$$u_t^\theta + u^r u_r^\theta + u^z u_z^\theta = -\frac{1}{r} u^r u^\theta, \tag{1.2a}$$

$$\omega_t^\theta + u^r \omega_r^\theta + u^z \omega_z^\theta = \frac{2}{r} u^\theta u_z^\theta + \frac{1}{r} u^r \omega^\theta, \tag{1.2b}$$

$$-\psi_{rr}^\theta - \psi_{zz}^\theta - \frac{1}{r}\psi_r^\theta + \frac{1}{r^2}\psi^\theta = \omega^\theta, \tag{1.2c}$$

$$u^r = -\psi_z^\theta, \quad u^z = \frac{1}{r}\psi^\theta + \psi_r^\theta. \tag{1.2d}$$

In the case of no swirl, i.e. $u^\theta \equiv 0$, the axisymmetric Euler equations are further simplified into:

$$\omega_t^\theta + u^r \omega_r^\theta + u^z \omega_z^\theta = \frac{1}{r} u^r \omega^\theta, \tag{1.3a}$$

$$-\psi_{rr}^\theta - \psi_{zz}^\theta - \frac{1}{r}\psi_r^\theta + \frac{1}{r^2}\psi^\theta = \omega^\theta, \tag{1.3b}$$

$$u^r = -\psi_z^\theta, \quad u^z = \frac{1}{r}\psi^\theta + \psi_r^\theta. \tag{1.3c}$$

When the initial condition for the angular vorticity ω^θ is smooth, it is well known that the 3D axisymmetric Euler equations with no swirl (1.3) will not develop finite-time blow-up [47]. Therefore, we consider (1.3) when the initial condition for the angular vorticity ω^θ is C^α Hölder continuous for a large range of α. By using an effective adaptive mesh method, we will provide convincing numerical evidences that the 3D axisymmetric Euler equations with no swirl and C^α initial voriticity with $0 < \alpha < 1/3$ develop potential finite-time self-similar blow-up.

We perform scaling analysis and use the dynamic rescaling formulation [21, 5, 8] to study the behavior of the potential self-similar blow-up. An operator splitting method is proposed to solve the dynamic rescaling formulation and the late time solution from the adaptive mesh method is used as our initial condition for the dynamic rescaling formulation. We observe rapid convergence to a steady state, which implies that this potential singularity is self-similar. We will demonstrate that this potential blow-up is stable with respect to the perturbation of initial data, suggesting that the underlying blow-up mechanism is generic and insensitive to the initial data. By introducing a parameter δ to control the stretching of the physical domain and the initial data in the z-axis, we find that the 3D Euler equations with C^α initial vorticity can develop potential finite-time blow-up when the Hölder exponent α is smaller than some α^*. This upper bound α^* can asymptotically approach $1/3$ as $\delta \to 0$. This result supports Conjecture 8 of [13].

We choose the following C^α initial data for ω^θ with a stretching parameter $\delta > 0$:

$$\omega_0^\theta = \frac{-12000\, r^\alpha \left(1 - r^2\right)^{18} \sin(2\pi\delta z)}{1 + 12.5\cos^2(\pi\delta z)}.$$

Note that the initial condition is a smooth and periodic function in z and is C^α in r. The velocity field u becomes $C^{1,\alpha}$ continuous. We further introduce the new variables:

$$\omega_1(r,z) = \frac{1}{r^\alpha}\omega^\theta(r,z), \quad \psi_1(r,z) = \frac{1}{r}\psi^\theta(r,z), \tag{1.4}$$

to remove the formal singularity in (1.3) near $r = 0$. In terms of the new variables (ω_1, ψ_1), the 3D axisymmetric Euler equations with no swirl have the following equivalent form

$$\omega_{1,t} + u^r\omega_{1,r} + u^z\omega_{1,z} = -(1-\alpha)\psi_{1,z}\omega_1, \tag{1.5a}$$

$$-\psi_{1,rr} - \psi_{1,zz} - \frac{3}{r}\psi_{1,r} = \omega_1 r^{\alpha-1}, \tag{1.5b}$$

$$u^r = -r\psi_{1,z}, \quad u^z = 2\psi_1 + r\psi_{1,r}. \tag{1.5c}$$

The above reformulation is crucial for us to perform accurate numerical computation of the potential singular solution and allow us to push the computation sufficiently close to the singularity time.

It is important to note that the initial condition for the rescaled vorticity field ω_1 is a smooth function of r and z. Using the above reformualtion enables us to resolve the potential singular solution sufficiently close to the potential singularity time. If we solve the original 3D Euler equations (1.3a)–(1.3c), it is extremely difficult to resolve the Hölder continuous vorticity even with an adaptive mesh, especially for small α. For this reason, we have not been able to compute the finite time singularity in Elgindi's work [15] since such a reformulation is not available for his initial data.

Compared with Elgindi's blow-up result [15], our potential blow-up scenario has very different scaling properties. The scaling factor c_l in our scenario increases with α and tends to infinity as α approaches α^*. In contrast, the scaling factor c_l in Elgindi's scenario is $1/\alpha$, which decreases with α and tends to infinity as α approaches 0. Another difference is that Elgindi's initial vorticity is C^α in both $\rho = \sqrt{r^2 + z^2}$ and z, while our initial vorticity is $C^{1,\alpha}$ continuous in ρ, but smooth in z.

There has been a number of theoretical analysis of the 3D Euler equations. The Beale-Kato-Majda (BKM) blow-up criterion [2, 17] gives a necessary and sufficient condition for the finite-time singularity for the smooth solutions of the 3D Euler equations at time T if and only if $\int_0^T \|\omega(\cdot,t)\|_{L^\infty}\mathrm{d}t = +\infty$. In [10], Constantin, Fefferman and Majda asserted that there will be no finite-time blow-up if the velocity u is uniformly bounded and the direction of vorticity $\xi = \omega/|\omega|$ is sufficiently regular (Lipschitz continuous) in an $O(1)$ domain containing the location of the maximum vorticity. Inspired by the work of [10], Deng-Hou-Yu developed a more localized non-blow-up criterion using a Lagrangian approach in [12].

There have been a number of numerical attempts in search of the potential finite-time blow-up. The finite-time blow-up in the numerical study was first reported by Grauer and Sideris [19] and Pumir and Siggia [41] for the 3D axisymmetric Euler equations. However, the later work of E and Shu [14] suggested that the finite-time blow-up in [19, 41] could be caused by numerical artifact. Kerr and his collaborators [24, 3] presented finite-time singularity formation in the Euler flows generated by a pair of perturbed anti-parallel vortex tubes. In [22], Hou and Li reproduced Kerr's computation using a similar initial condition with much higher resolutions and did not observe finite time blow-up. The maximum vorticity grows slightly slower than double exponential in time. Later on, Kerr confirmed in [25] that the solutions from [24] eventually converge to a super-exponential growth and are unlikely to lead to a finite-time singularity.

In [4, 45], Caflisch and his collaborators studied axisymmetric Euler flows with complex initial data and reported singularity formation in the complex plane. The review paper [18] lists a more comprehensive collection of interesting numerical results with more detailed discussions.

Due to the lack of stable structure in the potentially singular solutions, the previously mentioned numerical results remain inconclusive. In [35, 36], Luo and Hou reported that the 3D axisymmetric Euler equations with a smooth initial condition developed a self-similar finite time blow-up in the meridian plane on the boundary of $r = 1$, see also [37]. The Hou-Luo blow-up scenario has generated a great deal of interests in both the mathematics and fluid dynamics communities, and inspired a number of subsequent developments [28, 27, 26, 9, 7, 5, 8, 6].

The rest of this paper is organized as follows. In Section 2, we briefly introduce the numerical method. We present the evidence of the potential self-similar blow-up in Section 3, and provide the resolution study and scaling analysis. In Section 4 we use the dynamic rescaling method to provide further evidence of the potential blow-up for the case of $\alpha = 0.1$. In Section 5, we consider the potential finite-time blow-up in the general case of the Hölder exponent α, and introduce the anisotropic scaling parameter δ. The sensitivity of the potential blow-up to the initial data is considered in Section 6, and the comparison of our potential blow-up scenario with Elgindi's scenario in [15] is discussed in Section 7. Some concluding remarks are made in Section 8.

2. Problem set up and numerical method.

In this section, we give details about the setup of the problem, the initial data, the boundary conditions, and some basic properties of the equations, and our numerical method.

2.1. Boundary conditions and symmetries.

We consider (1.5) in a cylinder region

$$\mathcal{D}_{\text{cyl}} = \{(r, z) : 0 \le r \le 1\},$$

We impose a periodic boundary condition in z with period 1:

$$\omega_1(r, z) = \omega_1(r, z + 1), \quad \psi_1(r, z) = \psi_1(r, z + 1). \tag{2.1}$$

In addition, we enforce that (ω_1, ψ_1) are odd in z at $z = 0$:

$$\omega_1(r, z) = -\omega_1(r, -z), \quad \psi_1(r, z) = -\psi_1(r, -z). \tag{2.2}$$

And this symmetry will be preserved dynamically by the 3D Euler equations.

At $r = 0$, it is easy to see that $u^r(0, z) = 0$, so there is no need for the boundary condition for ω_1 at $r = 0$. Since $\psi^\theta = r\psi_1$ will at least be C^2-continuous, according to [32, 33], ψ^θ must be an odd function of r. Therefore, we impose the following pole condition for ψ_1

$$\psi_{1,r}(0,z) = 0. \tag{2.3}$$

We impose the no-flow boundary condition at the boundary $r = 1$:

$$\psi_1(1,z) = 0. \tag{2.4}$$

This implies that $u^r(1,z) = 0$. So there is no need to introduce a boundary condition for ω_1 at $r = 1$.

Due to the periodicity and the odd symmetry along the z direction, the equations (1.3) only need to be solved on the half-periodic cylinder

$$\mathcal{D} = \{(r,z) : 0 \le r \le 1, 0 \le z \le 1/2\}\,.$$

The above boundary conditions of $\mathcal{D}$ show that there is no transport of the flow across its boundaries. Indeed, we have

$$u^r = 0 \quad \text{on} \quad r = 0 \text{ or } 1, \quad \text{and} \quad u^z = 0 \quad \text{on} \quad z = 0 \text{ or } 1/2.$$

Thus, the boundaries of $\mathcal{D}$ behave like "impermeable walls".

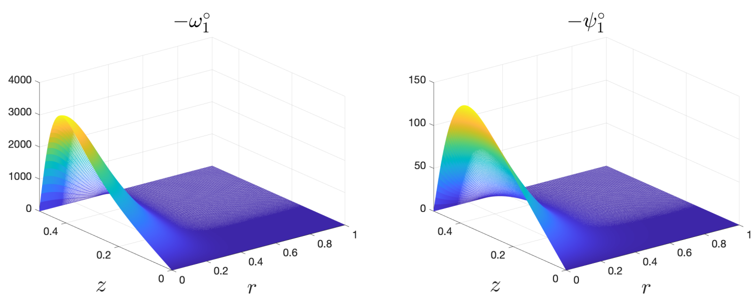

FIG. 1. *3D profiles of the initial value $-\omega_1^\circ$ and $-\psi_1^\circ$.*

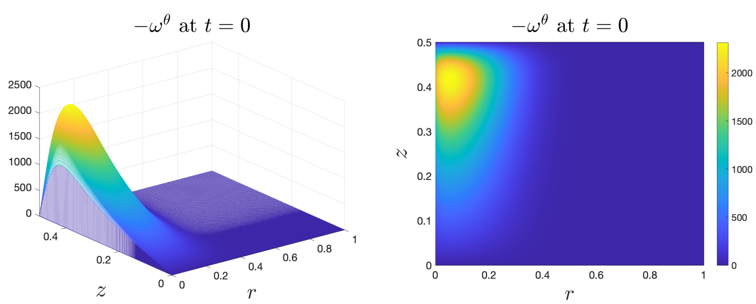

FIG. 2. *The initial data for the angular vorticity ω^θ.*

2.2. Initial data. Inspired by the potential blow-up scenario in [20], we propose the following initial data for ω_1 in $\mathcal{D}$,

$$\omega_1^\circ = \frac{-12000\left(1-r^2\right)^{18}\sin(2\pi z)}{1+12.5\cos^2(\pi z)}. \tag{2.5}$$

Later we will see in Section 6 that the self-similar singularity formation has some robustness to the choice of initial data. We solve the Poisson equation (1.5b) to get the initial value ψ_1° of ψ_1.

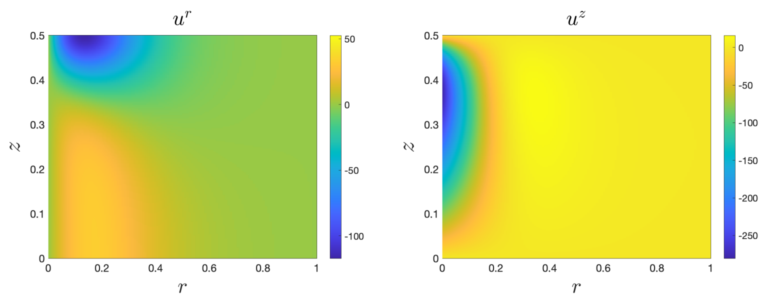

FIG. 3. *Initial velocity fields u^r and u^z.*

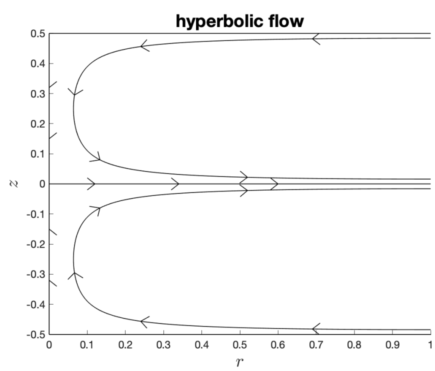

FIG. 4. *A heuristic diagram of the hyperbolic flow.*

The 3D profiles of $(\omega_1^\circ, \psi_1^\circ)$ can be found in Figure 1. Since most parts of ω_1° and ψ_1° are negative, we negate them for better visual effect when generating figures. In Figure 2, we show the 3D profile and pseudocolor plot of the angular vorticity ω^θ at $t = 0$. We can see that there is a sharp drop to zero of $-\omega^\theta$ near $r = 0$, which is due to the Hölder continuous of ω^θ at $r = 0$.

We plot the initial velocity field u^r and u^z in Figure 3. We can see that u^r is primarily positive near $z = 0$ and negative near $z = 1/2$ when r is small, and u^z is mainly negative when r is small. Such a pattern suggests a hyperbolic flow near $(r, z) = (0, 0)$ as depicted in the heuristic diagram Figure 4, which will extend periodically in z.

2.3. Self-similar solution. For nonlinear PDEs, people are particularly interested in studying self-similar blow-up solutions. A self-similar solution is when the local profile of the solution remains nearly unchanged in time after rescaling the spatial and the temporal variables of the physical solution. For example, for (1.5), the self-similar profile is the ansatz

$$\begin{aligned} \omega_1(x,t) &\approx \frac{1}{(T-t)^{c_\omega}}\Omega\left(\frac{x-x_0}{(T-t)^{c_l}}\right), \\ \psi_1(x,t) &\approx \frac{1}{(T-t)^{c_\psi}}\Psi\left(\frac{x-x_0}{(T-t)^{c_l}}\right), \end{aligned} \tag{2.6}$$

for some parameters c_ω, c_ψ, c_l, x_0 and T. Here T is considered as the blow-up time, and x_0 is the location of the self-similar blow-up. The parameters c_ω, c_ψ, c_l are called scaling factors.

It is also important to notice that the 3D Euler equations (1.1) enjoy the following scaling invariant property: if (u,ω,ψ) is a solution to (1.1), then $(u_{\lambda,\tau},\omega_{\lambda,\tau},\psi_{\lambda,\tau})$ is also a solution, where

$$u_{\lambda,\tau}(x,t)=\frac{\lambda}{\tau}u\left(\frac{x}{\lambda},\frac{t}{\tau}\right),\ \omega_{\lambda,\tau}(x,t)=\frac{1}{\tau}\omega\left(\frac{x}{\lambda},\frac{t}{\tau}\right),\ \psi_{\lambda,\tau}(x,t)=\frac{\lambda^2}{\tau}\psi\left(\frac{x}{\lambda},\frac{t}{\tau}\right),$$

and $\lambda>0$, $\tau>0$ are two constant scaling factors. In the case of the axisymmetric 3D Euler equations with no swirl (1.5), the scaling invariant property can be equivalently translated to: if (ω_1,ψ_1) is a solution of (1.5), then

$$\left\{\frac{1}{\lambda^\alpha\tau}\omega_1\left(\frac{x}{\lambda},\frac{t}{\tau}\right),\ \frac{\lambda}{\tau}\psi_1\left(\frac{x}{\lambda},\frac{t}{\tau}\right)\right\} \tag{2.7}$$

is also a solution.

If we assume the existence of the self-similar solution (2.6), then the new solutions in (2.7) should also admit the same ansatz, regardless of the values of λ and μ. As a result, we must have

$$c_\omega = 1+\alpha c_l, \quad c_\psi = 1-c_l. \tag{2.8}$$

Therefore, the self-similar profile (2.7) of (1.5) only has one degree of freedom, for example c_l, in the scaling factors. In fact, c_l cannot be determined by straightforward dimensional analysis.

As a consequence of the ansatz (2.6) and the scaling relation (2.8), we have

$$\|\omega^\theta(x,t)\|_{L^\infty}\sim\frac{1}{T-t},\quad \|\psi_{1,z}(x,t)\|_{L^\infty}\sim\frac{1}{T-t}, \tag{2.9}$$

which should always hold true regardless of the value of c_l.

2.4. Numerical method. Although the initial data are very smooth, the solutions of Euler equations quickly become very singular and concentrate in a rapidly shrinking region. Therefore, we use the adaptive mesh method to resolve the singular profile of the solutions. A detailed description of the adaptive mesh method can be found in [21, 37, 48]. Here we briefly introduce the idea behind the adaptive mesh method. The specific parameter setting used for the experiments in this work can be found in the appendix of [48].

The Euler equations (1.5) are originally posted as an initial-boundary value problem on the computational domain $(r,z)\in[0,1]\times[0,1/2]$. To capture the singular part of the solution, we introduce two variables $(\rho,\eta)\in[0,1]\times[0,1]$, and the maps

$$r=r(\rho),\quad z=z(\eta),$$

where we assume these two maps and their derivatives are all analytically known. We update these two maps from time to time according to some criteria and construct these two maps as monotonically increasing functions. We will use these two maps to map the physical domain in (r, z) to a computational domain in (ρ, η), so that $\omega_1(r(\rho), z(\eta))$ and $\psi_1(r(\rho), z(\eta))$ as functions of (ρ, η) are relatively smooth. Let n_ρ, n_η be the number of grid points along the r- and z- directions, respectively. And let $h_\rho = 1/n_\rho$, $h_\eta = 1/n_\eta$ be the mesh sizes along the r- and z- directions respectively. We place a uniform mesh on the computation domain of (ρ, η):

$$\mathcal{M}_{(\rho,\eta)} = \left\{(ih_\rho, jh_\eta) : 0 \le i \le n_\rho, 0 \le j \le n_\eta\right\}.$$

This is equivalent to covering the physical domain of (r, z) with the tensor-product mesh:

$$\mathcal{M}_{(r,z)} = \left\{(r(ih_\rho), z(jh_\eta)) : 0 \le i \le n_\rho, 0 \le j \le n_\eta\right\}.$$

With properly chosen maps of $r = r(\rho)$ and $z = z(\eta)$, the mesh $\mathcal{M}_{(r,z)}$ can focus on the singular part of the solution, so that the accuracy of the numerical solution can be greatly improved.

As we will see in the following sections, the singular part of the solutions will gradually move towards the origin. Thus we dynamically update the maps to accommodate the movement of the focused region. The update of the maps is based on an adaptive strategy that quantitatively locates the singular part of the solution and then decides the necessity to change the maps, as well as the parameters for the new maps. Once we update the maps, we interpolate the solutions from the old mesh to the new mesh and use the new computational domain. In our algorithm, we adopt a second-order implementation for our adaptive mesh method. In Section 3.3, we will perform resolution study to confirm the order of accuracy of our numerical method.

3. Numerical evidence for a potential self-similar singularity. In this section, we will focus on the case with Hölder exponent $\alpha = 0.1$, and provide numerical evidences for the potential self-similar singularity observed from the 3D axisymmetric Euler equations with no swirl and with Hölder continuous initial data. For the cases with different values of Hölder exponent α, we will present the results in Section 5.

3.1. Evidence for a potential singularity. On 1024×1024 spatial resolution, we use the adaptive mesh method to solve (1.5) with Hölder exponent $\alpha = 0.1$, until the time when the smallest adaptive mesh size gets close to the machine precision. The final time of the computation is at $t = 1.6524635 \times 10^{-3}$, after more than 6.5×10^4 iterations in time.

In Figure 5, we plot the dynamic growth of several important quantities of the solution. The magnitude of ω_1 has grown significantly, especially near the end of the computation. At the final time of the computation, $\|\omega_1\|_{L^\infty}$ has increased by a factor of around 5400, and $\|\omega\|_{L^\infty}$ has increased by a factor of more than 560. We also observe that the double logarithm curve of the maximum vorticity magnitude, $\log\log\|\omega\|_{L^\infty}$, maintains a super-linear growth, and the time integral $\int_0^t \|\omega(s)\|_{L^\infty}\mathrm{d}s$ has rapid growth with strong growth inertia close to the stopping time. This provides strong evidence for a potential finite-time blow-up of the 3D Euler equations by the Beale-Kato-Majda blow-up criterion.

In Figure 6, we plot the 3D profiles of ω_1, ψ_1, ω^θ, ψ^θ, u^r, and u^z at end of our computation. We can see that ω_1 is very concentrated near the origin, and so is ω^θ. Therefore, we zoom-in around the origin and plot the local near field profiles of ω_1, ψ_1, ω^θ, ψ^θ, u^r, and u^z in Figure 7. We observe that the "peak" of $-\omega_1$ locates at

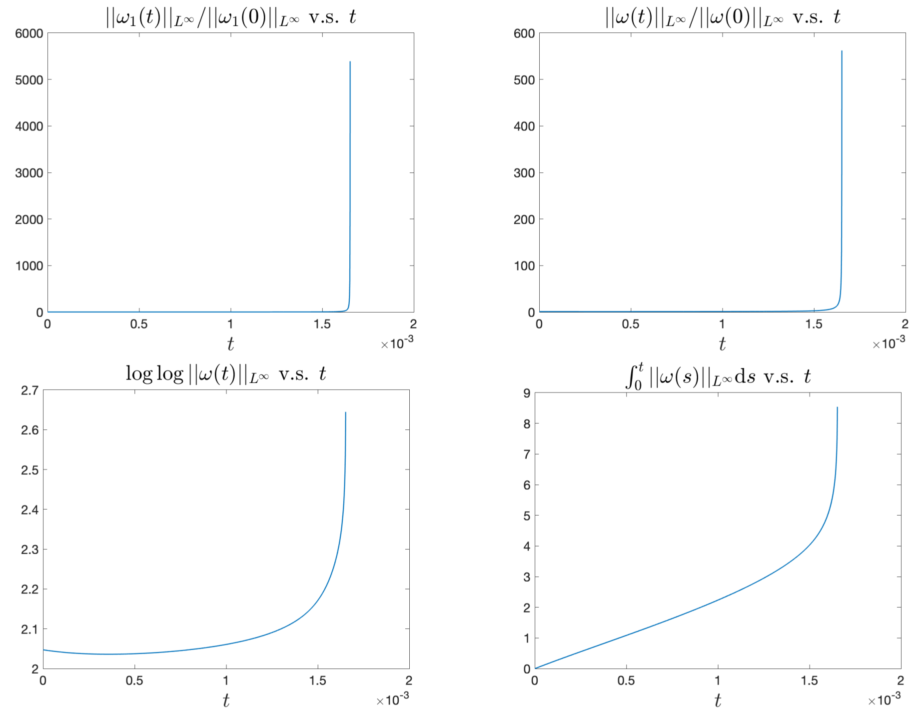

FIG. 5. *Curves of* $\|\omega_1\|_{L^\infty}$, $\|\omega\|_{L^\infty}$, $\log\log\|\omega\|_{L^\infty}$, $\int_0^t\|\omega(s)\|_{L^\infty}\mathrm{d}s$ *as functions of time* t.

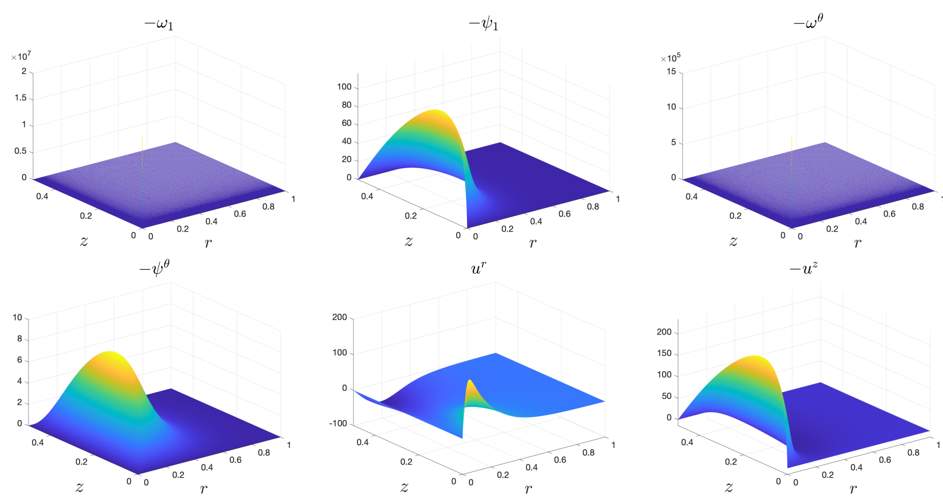

FIG. 6. *Profiles of* $-\omega_1$, $-\psi_1$, $-\omega^\theta$, $-\psi^\theta$, u^r *and* $-u^z$ *at* $t = 1.6524635 \times 10^{-3}$ *on the whole domain* $\mathcal{D}$.

the z-axis where $r = 0$, and is being pushed toward the origin as implied by the velocity field u^r, u^z. We denote by $(R_1(t), Z_1(t))$ the position at which $|\omega_1|$ achieves its maximum at time t. We have $R_1(t) = 0$. At $(R_1(t), Z_1(t))$, the radial velocity u^r is zero, and the axial velocity u^z is negative, which pushes $(R_1(t), Z_1(t))$ toward the origin.

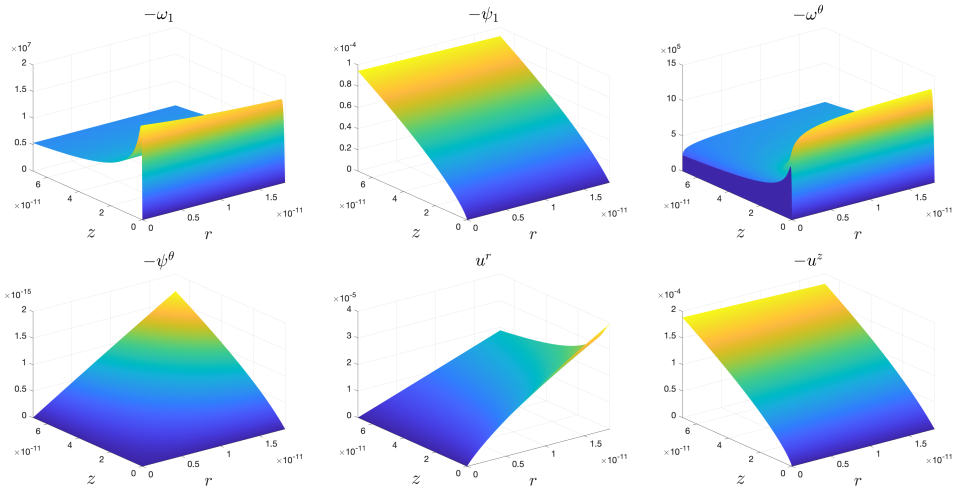

FIG. 7. *Zoomed-in profiles of $-\omega_1$, $-\psi_1$, $-\omega^\theta$, $-\psi^\theta$, u^r, and $-u^z$ near the origin* $(0,0)$ *at* $t = 1.6524635 \times 10^{-3}$.

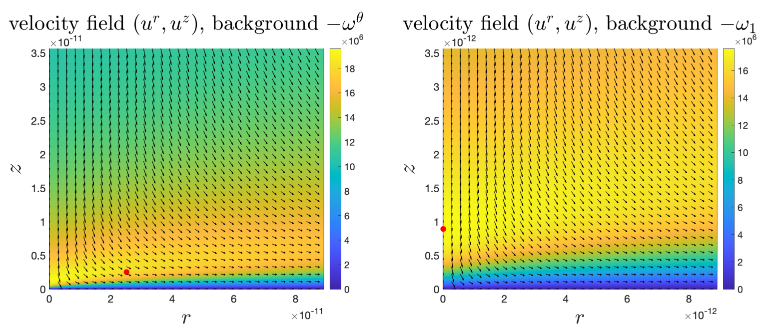

FIG. 8. *The local velocity field near the maximum of $-\omega^\theta$ and $-\omega_1$. The pseudocolor plot of $-\omega^\theta$ or $-\omega_1$ is the background, and the red dot is its maximum.*

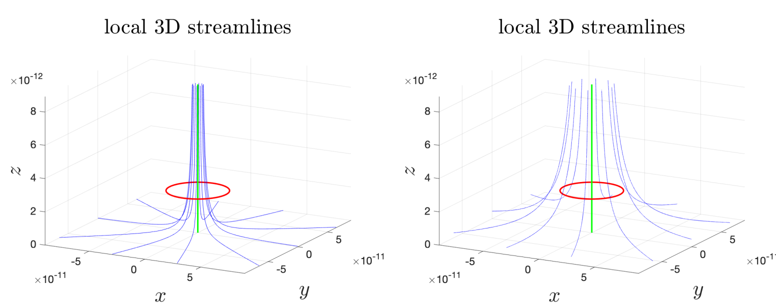

FIG. 9. *The local streamlines near the origin. The green pole is the z-axis, and the red ring is where $-\omega^\theta$ achieves its maximum.*

In Figure 8, we plot the local velocity field near the maximum of $-\omega^\theta$ and $-\omega_1$, respectively. We use the pseudocolor plots of $-\omega^\theta$ and $-\omega_1$ as the background, respectively for the figure in the left and the right subplots, and mark the maximum of $-\omega^\theta$ or $-\omega_1$ with the red dot. The velocity field demonstrates a clear hyperbolic structure as depicted by Figure 4. And the velocity field clearly pushes the maximum $(R_1(t), Z_1(t))$ of $-\omega_1$ toward the origin.

In Figure 9, we show the local streamlines near the maximum of $-\omega^\theta$ in $\mathbb{R}^3$. The maximum of $-\omega^\theta$ locates in the red ring centered at $(0, Z_1(t))$ along the z-axis. In the left figure, we plot a set of streamlines that travel through the maximum ring from top to bottom. And in the right figure, we plot a set of streamlines that travel around the maximum ring from top to bottom. From Figure 9, we notice that the streamlines are axisymmetric, and do not form swirl around the z-axis.

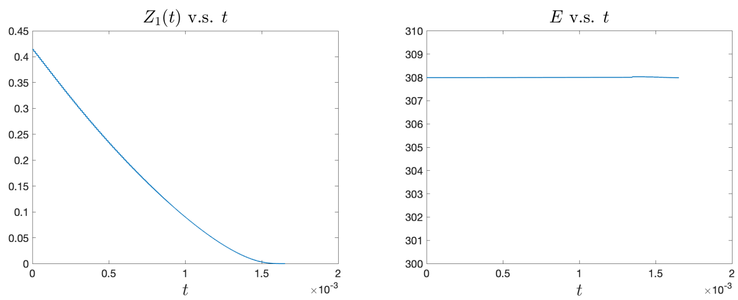

FIG. 10. *Curves of Z_1 and E as functions of time t.*

In Figure 10, we show the curve of the maximum location of $-\omega_1$, Z_1 and the kinetic energy, E as functions of time. We can also see that $Z_1(t)$ monotonically decreases to zero with t. The curve of $Z_1(t)$ seems to be convex, especially in time windows close to the stopping time. We refer to Section 3.4 for more study of the behavior of $Z_1(t)$. The kinetic energy E, which is defined as

$$E = \frac{1}{2}\int_{\mathcal{D}} |u|^2 \,\mathrm{d}x = \pi \int_0^1 \int_0^{1/2} \left(|u^r|^2 + |u^z|^2\right) r\mathrm{d}r\mathrm{d}z,$$

for our axisymmetric case with no swirl, is a conservative quantity of the 3D Euler equations. In Figure 10, we can see that there is little change of the kinetic energy E as a function of time t. In fact, the major reason for the change of E in our computation is due to the update of adaptive mesh, where we need to interpolate ω_1 and ψ_1 from an old mesh to a new mesh. Since the new adaptive mesh will be more focusing on the near field around the origin, the far field velocity field might lose some accuracy, leading to a change in the kinetic energy E. However, such an update of adaptive mesh occurs only 35 times out of the total 65000 iterations in time, and the change in the kinetic energy E in each update is negligible. By the end of the computation, the change in the kinetic energy E is at most 1.4×10^{-4} of the magnitude of E.

3.2. Evidence for a potential self-similar blow-up. We observe a potential self-similar blow-up in our numerical solution. To check the self-similar property, we visualize the local profile of the rescaled ω_1 near the origin. Recall that $(0, Z_1)$ is the maximum location of $-\omega_1$, we define

$$\hat{\omega}_1(\xi, \zeta, t) = \omega_1\left(Z_1(t)\xi, Z_1(t)\zeta, t\right)/\|\omega_1(t)\|_{L^\infty},$$

as the rescaled version of ω_1. The above definition rescales the magnitude of $|\hat{\omega}_1|$ to 1, and rescales the maximum location of $|\hat{\omega}_1|$ to $(\xi,\zeta) = (0,1)$. We plot the profiles of $-\hat{\omega}_1$ near the origin at different time instants and the contours of $-\hat{\omega}_1(\xi,\zeta)$ at different times in Figure 11. The profile of $-\hat{\omega}_1$ seems to change slowly in the late time, indicating a potential self-similar structure of the blow-up profile near the origin. In other words, $x_0 = 0$ in the self-similar ansatz (2.6).

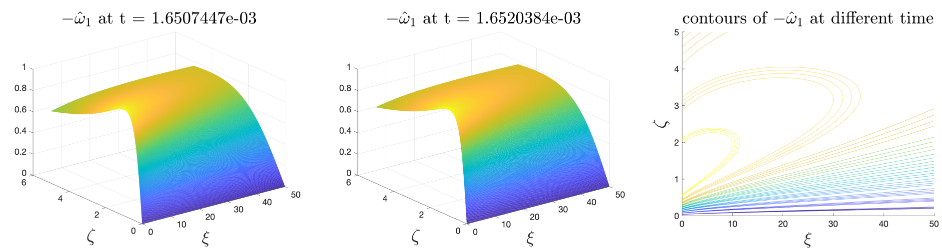

FIG. 11. *Left and middle: Local profiles of $-\hat{\omega}_1$ at $t = \{1.6507447\,,\ 1.6520384\} \times 10^{-3}$. Right: Local contours of $-\hat{\omega}_1$ at $t = \{1.6507447\,,\ 1.6512953,\ 1.6517173,\ 1.6520384\} \times 10^{-3}$.*

In Figure 12, we plot the cross sections of $-\hat{\omega}_1$ at $\xi = 0$ and $\zeta = 1$. The cross section at $\xi = 0$ shows a good potential for a self-similar blow-up, while the cross section at $\zeta = 1$ shows that the blow-up profile has not converged to a self-similar profile yet. This is reasonable because although we are very close to the potential blow-up time, the strong collapsing along the z-direction and the effect of round-off errors prevent us from continuing the computation. We refer to Section 4 where we use the dynamic rescaling method and indeed observe numerically the convergence to the potential self-similar profile.

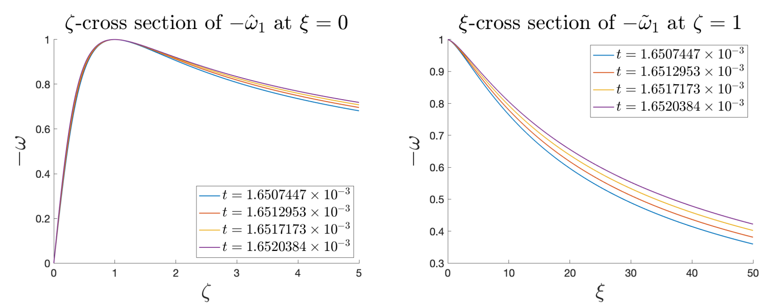

FIG. 12. *Cross sections of $-\hat{\omega}_1$ at different times.*

3.3. Resolution study. We perform resolution study on the numerical solutions of (1.5) to confirm the accuracy of our numerical solutions. We first simulate the equations on spatial resolutions of $256k \times 256k$ with $k = 1, 2, \ldots, 6$. The highest resolution we used is 1536×1536. Next, for the numerical solution at resolution $256k \times 256k$, we compute its sup-norm relative error in several chosen quantities at selected time instants using the numerical solution at resolution $256(k+1) \times 256(k+1)$ as the reference, for $k = 1, 2, \ldots, 5$. Finally, we use the relative error obtained above to estimate the convergence order of the numerical method.

We consider two types of quantities. The first type is the function of the solutions. Here we consider the magnitude of ω_1, $\|\omega_1\|_{L^\infty}$, the maximum norm of vorticity, $\|\omega\|_{L^\infty}$, and the kinetic energy, E. We remark that $\|\omega_1\|_{L^\infty}$ and $\|\omega\|_{L^\infty}$ only depend on the local field near the origin, and E should be considered as a global quantity. The second type is the vector fields of ω_1, ψ_1, u^r, and u^z that are actively participating in the simulated system (1.5).

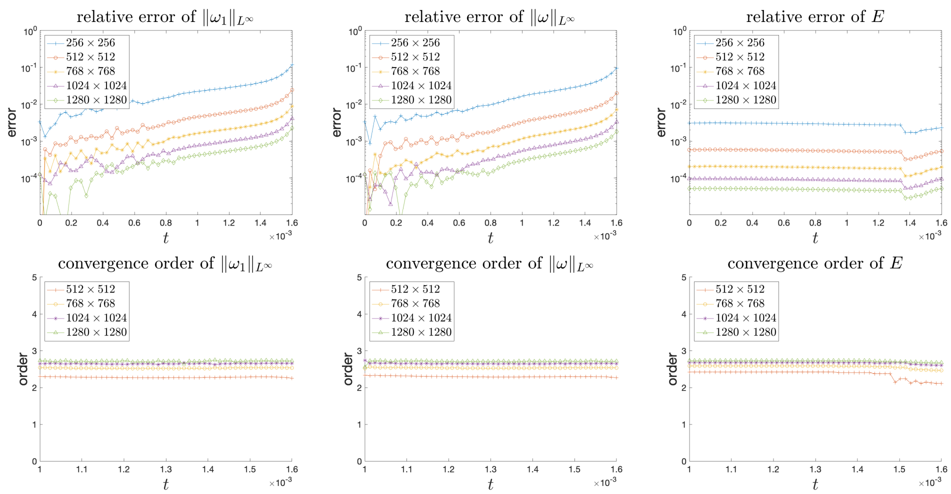

FIG. 13. *Relative errors and convergence orders of $\|\omega_1\|_{L^\infty}$, $\|\omega\|_{L^\infty}$, and E in sup-norm.*

For each quantity, we use q_k to represent the estimate we get at resolution $256k \times 256k$. Then the sup-norm relative error e_k is defined as

$$e_k = \|q_k - q_{k+1}\|_{L^\infty} / \|q_{k+1}\|_{L^\infty}.$$

If q_k is a vector field, we first interpolate it to the reference resolution $256(k+1) \times 256(k+1)$, and then compute the relative error as above. The convergence order of the error β_k at this resolution can be estimated via

$$\beta_k = \log\left(\frac{e_{k-1}}{e_k}\right) \Big/ \log\left(\frac{k}{k-1}\right).$$

In Figure 13, we plot the relative error of the quantities $\|\omega_1\|_{L^\infty}$, $\|\omega\|_{L^\infty}$ and E for $t \in \left[0, 1.6 \times 10^{-3}\right]$, and the convergence order of the error in the late time $t \in \left[1 \times 10^{-3}, 1.6 \times 10^{-3}\right]$. We observe a numerical convergence with order slightly higher than 2. The convergence order is quite stable in the time interval of our computation.

In Table 1, we list the relative error and convergence order of the vector fields at $t = 1.6 \times 10^{-3}$. The convergence order stays well above 2, suggesting at least a second-order convergence for our numerical solver of the 3D Euler equations.

3.4. Scaling analysis. In this section, we quantify the scaling property of the potential blow-up observed in our computation. This scaling analysis will give more supporting evidence that the potential blow-up satisfies the Beale-Kato-Majda blow-up criterion. It also uncovers more properties of the potential blow-up.

As discussed in (2.6) of Section 2.3, if there is a self-similar blow-up, the scaling invariant property of the 3D Euler equations will ensure that $\|\omega\|_{L^\infty} \sim 1/(T-t)$ and $\|\psi_{1,z}\|_{L^\infty} \sim 1/(T-t)$. Therefore, we examine this property by regressing $\|\omega\|_{L^\infty}^{-1}$ and $\|\psi_{1,z}\|_{L^\infty}^{-1}$ again t, respectively. More specifically, for a quantity v, which is either $\|\omega\|_{L^\infty}^{-1}$ or $\|\psi_{1,z}\|_{L^\infty}^{-1}$, we perform the least square fitting of the model

$$v \sim a \cdot (b - t),$$

TABLE 1
Relative errors and convergence orders of ω_1, ψ_1, u^r and u^z in sup-norm.

mesh size	Sup-norm relative error at $t = 1.6 \times 10^{-3}$			
	ω_1	order	ψ_1	order
256×256	2.545×10^{-1}	-	5.912×10^{-3}	-
512×512	5.478×10^{-2}	2.216	1.168×10^{-3}	2.340
768×768	1.969×10^{-2}	2.524	4.136×10^{-4}	2.560
1024×1024	9.189×10^{-3}	2.655	1.926×10^{-4}	2.656
1280×1280	5.008×10^{-3}	2.720	1.050×10^{-4}	2.719

mesh size	Sup-norm relative error at $t = 1.6 \times 10^{-3}$			
	u^r	order	u^z	order
256×256	2.035×10^{-2}	-	8.095×10^{-3}	-
512×512	3.954×10^{-3}	2.364	1.533×10^{-3}	2.310
768×768	1.405×10^{-3}	2.552	5.793×10^{-4}	2.556
1024×1024	6.540×10^{-4}	2.658	2.699×10^{-4}	2.655
1280×1280	3.594×10^{-4}	2.682	1.472×10^{-4}	2.719

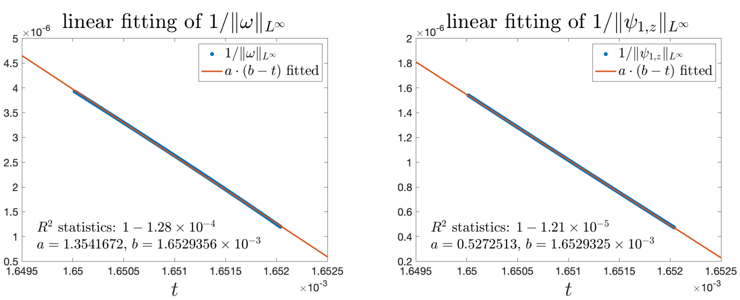

FIG. 14. *Linear fitting of $1/\|\omega\|_{L^\infty}$ and $1/\|\psi_{1,z}\|_{L^\infty}$ with time.*

in searching for constants a and b, where a is the negated slope of the fitted line, and b can be considered as the estimate time of the blow-up. In Figure 14, we visualize the data points and the fitted line using data between $t = 1.6500174 \times 10^{-3}$ and $t = 1.6520384 \times 10^{-3}$. The R^2 of the fitting between $\|\omega\|_{L^\infty}^{-1}$ and t is $1 - 1.28 \times 10^{-4}$, and the R^2 of the fitting between $\|\psi_{1,z}\|_{L^\infty}^{-1}$ and t is $1 - 1.21 \times 10^{-5}$. Such high R^2 values show strong linear relation between $\|\omega\|_{L^\infty}^{-1}$, $\|\psi_{1,z}\|_{L^\infty}^{-1}$ and t. Moreover, the fittings of the two quantities estimate the blow-up time to be $b = 1.6529356 \times 10^{-3}$ and $b = 1.6529325 \times 10^{-3}$ respectively. These two blow-up times agree with each other up to 6 digits. Therefore, Figure 14 provides further evidence that the 3D Euler equations develop a potential finite-time singularity.

We next move to fit the scaling factors c_l and c_ω used in the self-similar ansatz (2.6) of the solutions. Since the functions Ω and Ψ are time-independent in (2.6), we should have that

$$Z_1 \sim (T - t)^{c_l}, \quad \|\omega_1\|_{L^\infty}^{-1} \sim (T - t)^{c_\omega},$$

where we recall that $Z_1 = Z_1(t)$ is the z-coordinate of the maximum location of $-\omega_1$. Due to the unknown powers c_l and c_ω, the direct fitting of the above model is nonlinear. Therefore, we turn to a searching algorithm for the power variable. Specifically, for a quantity v, that is either Z_1 or $\|\omega_1\|_{L^\infty}^{-1}$, we search for a power c

such that the linear regression of

$$v^{1/c} \sim a \cdot (b - t),$$

has the largest R^2 value up to some error tolerance. We will start with a guessed window of the power c, and then exhaust the value of c within the window up to some error tolerance, and choose c with the largest R^2 value. If the optimal c we searched falls on the boundary of the current window, we then adaptively adjust the window size and location, and repeat the above procedure. When the optimal searched c falls within the interior of the window, we stop the searching.

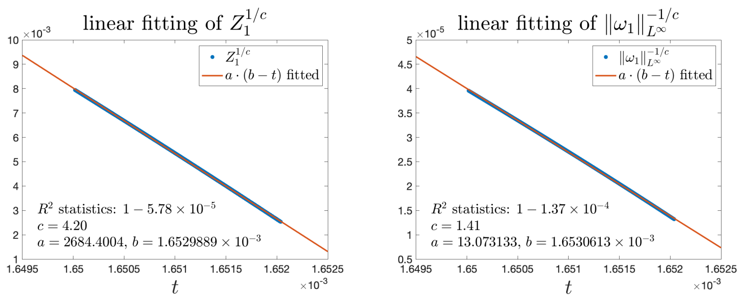

Fig. 15. *Linear fitting of* $Z_1^{1/c}$ *and* $\|\omega_1\|_{L^\infty}^{-1/c}$ *with time.*

In Figure 15, we demonstrate the result of the searching. We can see that with the chosen c, the linear regression achieves a very high R^2 value, suggesting a strong linear relation. The relative error between the estimated blow-up time and the previous estimate smaller than 7.8×10^{-5}. Moreover, the searching suggests that $c_l \approx 4.20$ and $c_\omega \approx 1.41$, and these estimated values of c_l and c_ω satisfy the scaling relation $c_\omega = 1 + \alpha c_l$ in (2.8) approximately.

It is worth emphasizing that the estimated c_l is well above 1, and this explains the convex curve of $Z_1(t)$ as observed in Figure 10 in Section 3.1.

We remark that we did not perform the searching algorithm with $\|\psi_1\|_{L^\infty}$ to find out the scaling factor c_ψ, so that we could check the other scaling relation $c_\psi = 1 - c_l$ in (2.8). This is because $\|\psi_1\|_{L^\infty}$ is mainly affected by the far field behavior of ψ_1, as shown in Figure 6. However, the self-similar ansatz (2.6) is only valid in the near field, so such fitting is meaningless. In fact, the good fitting between $\|\psi_{1,z}\|_{L^\infty}^{-1}$ and t already implies that $c_\psi = 1 - c_l$, because the self-similar ansatz suggests that $\|\psi_{1,z}\|_{L^\infty}^{-1} \sim (T-t)^{c_\psi + c_l}$.

Finally, we perform the above fitting of different quantities using different spatial resolutions, and summarize the results in Table 2. We can see that the fitting has excellent quality at all spatial resolutions, and the fitted parameters are consistent across different spatial resolutions.

4. The dynamic rescaling formulation. In order to better study the potential self-similar singularity as we have observed in Section 3.2, we add extra scaling terms to (1.5) and write

$$\tilde\omega_{1,\tau} + \left(\tilde c_l \xi + \tilde u^\xi\right) \tilde\omega_{1,\xi} + \left(\tilde c_l \zeta + \tilde u^\zeta\right) \tilde\omega_{1,\zeta} = \Big(c_\omega - (1-\alpha)\tilde\psi_{1,\zeta}\Big) \tilde\omega_1, \tag{4.1a}$$

$$-\tilde\psi_{1,\xi\xi} - \tilde\psi_{1,\zeta\zeta} - \frac{3}{\xi}\tilde\psi_{1,\xi} = \tilde\omega_1 \xi^{\alpha-1}, \tag{4.1b}$$

$$\tilde u^\xi = -\xi \tilde\psi_{1,\zeta}, \quad \tilde u^\zeta = 2\tilde\psi_1 + \xi\tilde\psi_{1,\xi}, \tag{4.1c}$$

TABLE 2
Fitting results of $\|\omega\|_{L^\infty}^{-1}$, $\|\psi_{1,z}\|_{L^\infty}^{-1}$, Z_1 and $\|\omega_1\|_{L^\infty}^{-1}$ at different mesh sizes.

mesh size	$1/\|\omega\|_{L^\infty}$		$1/\|\psi_{1,z}\|_{L^\infty}$	
	$10^3 \times b$	R^2	$10^3 \times b$	R^2
1024×1024	1.6529356	0.99987	1.6529325	0.99999
1280×1280	1.6527953	1.00000	1.6528189	1.00000
1536×1536	1.6525824	1.00000	1.6527396	1.00000

mesh size	Z_1			$1/\|\omega_1\|_{L^\infty}$		
	c	$10^3 \times b$	R^2	c	$10^3 \times b$	R^2
1024×1024	4.20	1.6529889	0.99994	1.41	1.6530613	0.99986
1280×1280	4.21	1.6527877	0.99999	1.42	1.6527894	1.00000
1536×1536	4.25	1.6526864	1.00000	1.41	1.6526953	1.00000

where $\tilde{c}_l = \tilde{c}_l(\tau)$, $\tilde{c}_\omega = \tilde{c}_\omega(\tau)$ are scalar functions of τ. In (4.1a), the terms $\tilde{c}_l \xi \partial_\xi$ and $\tilde{c}_l \zeta \partial_\zeta$ stretch the solutions in space to maintain a finite support of the self-similar blow-up solution. The term $\tilde{c}_\omega \tilde{\omega}_1$ acts as a damping term to ensure that the magnitude of $\tilde{\omega}_1$ remains finite. The combined effect of these terms dynamically rescales the solution to capture the potential self-similar profile. Such dynamic rescaling strategy has widely been used in the study of singularity formation of nonlinear Schrödinger equations as in [39, 30, 31, 29, 40]. And recently it has been used to study singularity formation of the 3D Euler equations as in [21, 5, 8].

If we define

$$\tilde{c}_\psi(\tau) = \tilde{c}_\omega(\tau) + (1+\alpha)\tilde{c}_l(\tau), \tag{4.2}$$

we can check that (4.1) admits the following solution

$$\begin{aligned} \tilde{\omega}_1(\xi,\zeta,\tau) &= \tilde{C}_\omega(\tau)\omega_1\left(\tilde{C}_l(\tau)\xi, \tilde{C}_l(\tau)\zeta, t(\tau)\right), \\ \tilde{\psi}_1(\xi,\zeta,\tau) &= \tilde{C}_\psi(\tau)\psi_1\left(\tilde{C}_l(\tau)\xi, \tilde{C}_l(\tau)\zeta, t(\tau)\right), \end{aligned} \tag{4.3}$$

where (ω_1, ψ_1) is the solution to (1.5), and

$$\begin{aligned} &\tilde{C}_\omega(\tau) = \exp\left(\int_0^\tau \tilde{c}_\omega(s)\mathrm{d}s\right), \quad \tilde{C}_\psi(\tau) = \exp\left(\int_0^\tau \tilde{c}_\psi(s)\mathrm{d}s\right), \\ &\tilde{C}_l(\tau) = \exp\left(-\int_0^\tau \tilde{c}_l(s)\mathrm{d}s\right), \quad t'(\tau) = \tilde{C}_\psi(\tau)\tilde{C}_l(\tau) = \tilde{C}_\omega(\tau)\tilde{C}_l^{-\alpha}(\tau). \end{aligned}$$

The new equations (4.1) leave us with two degrees of freedom: we are free to choose $\{\tilde{c}_l(\tau), \tilde{c}_\omega(\tau)\}$. This allows us to impose the following normalization conditions

$$\tilde{\omega}_1(0,1,\tau) = -1, \quad \tilde{\omega}_{1,\zeta}(0,1,\tau) = 0, \quad \text{for } \tau \geq 0. \tag{4.4}$$

One way to enforce the normalization conditions, as used in many literatures like [21, 34], is to first enforce them at $\tau = 0$ using the scaling invariant relation (2.7), and then enforce their time derivatives to be zero

$$\frac{\partial}{\partial\tau}\tilde{\omega}_1(0,1,\tau) = 0, \quad \frac{\partial}{\partial\tau}\tilde{\omega}_{1,\zeta}(0,1,\tau) = 0, \quad \text{for } \tau \geq 0. \tag{4.5}$$

Using (4.1a), the above conditions are equivalent to

$$\begin{aligned}\tilde{c}_l(\tau) =& -2\tilde{\psi}_1(0,1,\tau) - (1-\alpha)\tilde{\psi}_{1,\zeta\zeta}(0,1,\tau)\frac{\tilde{\omega}_1(0,1,\tau)}{\tilde{\omega}_{1,\zeta\zeta}(0,1,\tau)},\\ \tilde{c}_\omega(\tau) =& (1-\alpha)\tilde{\psi}_{1,\zeta}(0,1,\tau).\end{aligned} \tag{4.6}$$

However, it is hard to evaluate (4.6) accurately, because it requires calculating second-order derivatives. More importantly, due to the complicated nonlinear nature of (4.1a), even if (4.6) can be accurately evaluated, the temporal discretization (Runge-Kutta method) makes it difficult to enforce (4.4) exactly for the next time step. As a result, imposing (4.5) is not as helpful to preserve the normalization conditions (4.4) in the following time steps. The maximum magnitude and location will gradually change in time, which makes it difficult to compute the self-similar profile numerically.

4.1. The operator splitting strategy. To enforce the normalization conditions (4.4) accurately at every time step, we utilize the operator splitting method and rewrite (4.1a) as

$$\tilde{\omega}_{1,\tau} = F(\tilde{\omega}_1) + G(\tilde{\omega}_1), \tag{4.7}$$

where $F(\tilde{\omega}_1) = -\tilde{u}^\xi\tilde{\omega}_{1,\xi} - \tilde{u}^\zeta\tilde{\omega}_{1,\zeta} - (1-\alpha)\tilde{\psi}_{1,\zeta}\tilde{\omega}_1$ contains the original terms in (1.5a), and $G(\tilde{\omega}_1) = -\tilde{c}_l\xi\tilde{\omega}_{1,\xi} - \tilde{c}_l\zeta\tilde{\omega}_{1,\zeta} + \tilde{c}_\omega\tilde{\omega}_1$ is the linear part that controls the rescaling. Here we view $\tilde{\psi}_1$ as a function of $\tilde{\omega}_1$ through the Poisson equation (4.1b). The operator splitting method allows us to solve (4.1a) by solving $\tilde{\omega}_{1,\tau} = F(\tilde{\omega}_1)$ and $\tilde{\omega}_{1,\tau} = G(\tilde{\omega}_1)$ alternatively.

We can use the standard Runge-Kutta method to solve $\tilde{\omega}_{1,\tau} = F(\tilde{\omega}_1)$. As for $\tilde{\omega}_{1,\tau} = G(\tilde{\omega}_1)$, we notice that there is a closed form solution for the initial value problem

$$\tilde{\omega}_1(\xi,\zeta,\tau) = \tilde{C}_\omega(\tau)\tilde{\omega}_1\left(\tilde{C}_l(\tau)\xi, \tilde{C}_l(\tau)\zeta, 0\right), \tag{4.8}$$

where $\tilde{C}_\omega(\tau) = \exp\left(\int_0^\tau \tilde{c}_\omega(s)\mathrm{d}s\right)$ and $\tilde{C}_l(\tau) = \exp\left(-\int_0^\tau \tilde{c}_l(s)\mathrm{d}s\right)$.

In the first step, solving $\tilde{\omega}_{1,\tau} = F(\tilde{\omega}_1)$ will violate the normalization conditions (4.4). But we will correct this error in the second step by solving $\tilde{\omega}_{1,\tau} = G(\tilde{\omega}_1)$ with a smart choice of $\tilde{C}_l$ and $\tilde{C}_\omega$ in (4.8). In other words, at every time step when we solve $\tilde{\omega}_{1,\tau} = G(\tilde{\omega}_1)$, we can exactly enforce (4.4) by properly choosing $\tilde{C}_l$ and $\tilde{C}_\omega$ in (4.8). We could also adopt Strang's splitting [46] for better temporal accuracy.

4.2. Numerical settings. Now we numerically solve the dynamic rescaling formulation (4.1). For the initial condition, we use the solution obtained from the final iteration of the adaptive mesh method in Section 3.1, and use the relation (2.7) to enforce the normalization conditions (4.5). Now that the maximum location of $\tilde{\omega}_1$ is pinned at $(\xi,\zeta) = (0,1)$, we focus on a large computational domain

$$\mathcal{D}' = \left\{(\xi,\zeta) : 0 \le \xi \le 1\times 10^5, 0 \le \zeta \le 5\times 10^4\right\}.$$

This choice of the computational domain implies that the dynamic rescaling formulation effectively solves the original equations in the domain $(r,z) \in [0, 100000Z_1] \times [0, 50000Z_1]$.

We adopt the boundary conditions and symmetry of (1.5) in Section 2.1, except the far field boundary conditions for $\tilde{\psi}_1$. Due to extra stretching terms, the far field

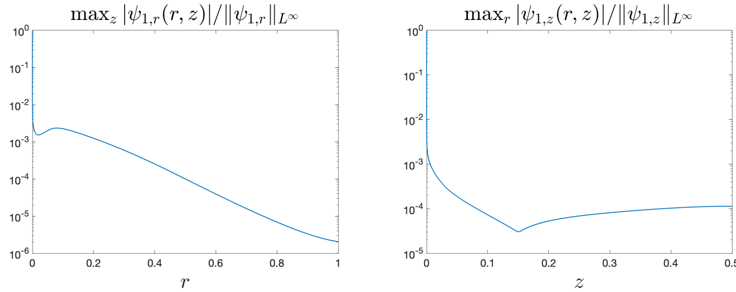

FIG. 16. *Decay of the derivatives of* ψ_1.

boundary for $\tilde{\psi}_1$ will no longer correspond to the far field boundary for ψ_1, namely $r = 1$ and $z = 1/2$. However, we notice that $\psi_{1,r}$ decays rapidly with respect to r, and $\psi_{1,z}$ decays rapidly with respect to z. For example, Figure 16 shows the decay of $\psi_{1,r}$ as $r \to 1$ and the decay of $\psi_{1,z}$ as $z \to 1/2$ for the solution to (1.5) at $t = 1.6524635 \times 10^{-3}$. Therefore, it is reasonable to impose the zero Neumann boundary condition at the far field boundaries of $\mathcal{D}'$: $\xi = 100000$ and $\zeta = 50000$. Due to the size of the computation domain $\mathcal{D}'$ and the presence of the vortex stretching terms, the error introduced by this boundary condition will have little influence on the near field around $(\xi, \zeta) = (0, 1)$.

We remark that we still need the adaptive mesh in the r- and z-directions, because we not only need to cover a very large field, but also need to focus around $(\xi, \zeta) = (0, 1)$. The adaptive mesh that we use to solve the dynamic rescaling formulation will not change during the computation, since the dynamically rescaled vorticity has its maximum location fixed at $(\xi, \zeta) = (0, 1)$ for all times instead of traveling toward the origin.

4.3. Convergence to the steady state. We solve (4.1) until it converges to a steady state. In Figure 17, we monitor how the normalization conditions (4.5) are enforced on the left. The two normalized quantities are essentially fixed at 1, and in fact, they deviate from 1 by less than 5.14×10^{-4}. We view the system (4.1) as an ODE of $\tilde{\omega}_1$ as in (4.7), and plot the relative strength of the time derivative

$$\|\tilde{\omega}_{1,\tau}\|_{L^\infty}/\|\tilde{\omega}_1\|_{L^\infty} = \|F(\tilde{\omega}_1) + G(\tilde{\omega}_1)\|_{L^\infty}/\|\tilde{\omega}_1\|_{L^\infty},$$

as a function of time τ in the right subplot of Figure 17. This relative strength of the time derivative has a decreasing trend and drops below 8.18×10^{-6} near the end of the computation, which implies that we are very close to the steady state.

When the solution of (4.1) converges to a steady state, $\tilde{\omega}_1$ and $\tilde{\psi}_1$ are independent of the time τ. Therefore, we should have the following relation from (4.3)

$$\omega_1(r,z,t) \sim \tilde{C}_\omega^{-1}(\tau(t))\tilde{\omega}_1\left(\tilde{C}_l^{-1}(\tau(t))r, \tilde{C}_l^{-1}(\tau(t))z\right),$$
$$\psi_1(r,z,t) \sim \tilde{C}_\psi^{-1}(\tau(t))\tilde{\psi}_1\left(\tilde{C}_l^{-1}(\tau(t))r, \tilde{C}_l^{-1}(\tau(t))z\right),$$

where $\tau = \tau(t)$ is the rescaled time variable. Comparing the above relation with the ansatz stated in (2.6), we conclude that

$$c_l = -\frac{\tilde{c}_l}{\tilde{c}_\omega + \alpha\tilde{c}_l}, \quad c_\omega = \frac{\tilde{c}_\omega}{\tilde{c}_\omega + \alpha\tilde{c}_l}, \quad c_\psi = \frac{\tilde{c}_\psi}{\tilde{c}_\omega + \alpha\tilde{c}_l}. \tag{4.9}$$

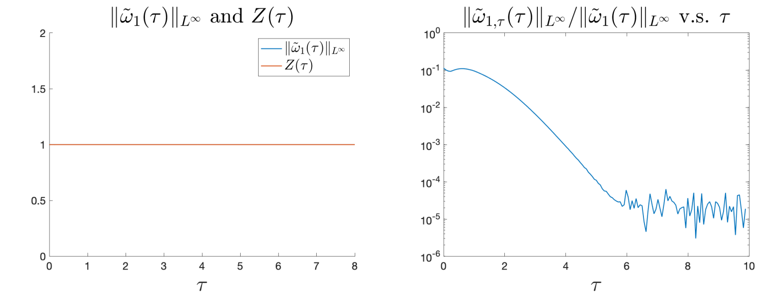

FIG. 17. *Left: curves of the normalized quantities $\|\tilde{\omega}_1(\tau)\|_{L^\infty}$ and $Z_1(\tau)$. Right: Curve of the relative time derivative strength $\|\tilde{\omega}_{1,\tau}(\tau)\|_{L^\infty}/\|\tilde{\omega}_1(\tau)\|_{L^\infty}$.*

We remark that assuming (4.2), the above relation naturally guarantees that the scaling relation (2.8) holds true.

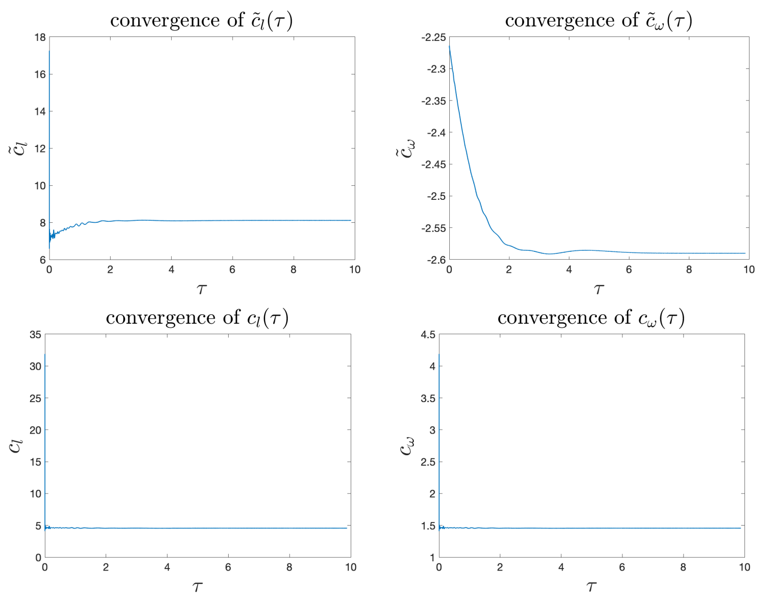

FIG. 18. *Convergence curves of the scaling factors using dynamic rescaling method. Top row: $\tilde{c}_l$ and $\tilde{c}_\omega$. Bottom row: c_l and c_ω.*

In Figure 18, we show the curves of scaling factors $\tilde{c}_l$, $\tilde{c}_\omega$ for the dynamic rescaling formulation (4.1) and c_l, c_ω for the self-similar ansatz (2.6). We observe a relatively fast convergence to the steady state as time increases. The converged values $c_l = 4.549$ and $c_\omega = 1.455$ are close to the approximate values obtained in Section 3.4. Moreover, they also satisfy the relation (2.8).

The approximate steady states of $\tilde{\omega}_1$ and $\tilde{\psi}_1$ are plotted in Figure 19. We see that both $\tilde{\omega}_1$ and $\tilde{\psi}_1$ are relatively flat in ξ, suggesting a possible 1D structure of their profiles. While both functions have weak dependence on ξ, $-\tilde{\omega}_1$ seems to tilt up around $\xi = 0$ a little bit. The shape of the steady states looks similar to the shape of the profiles we obtained via the adaptive mesh at the stopping time in Figure 7.

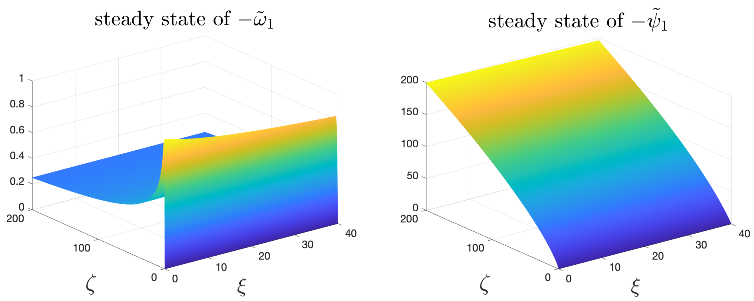

FIG. 19. *Steady states of $-\tilde{\omega}_1$ and $-\tilde{\psi}_1$.*

5. The Hölder exponent and the anisotropic scaling in the potential blow-up. Starting this section, we will no longer fix the Hölder exponent $\alpha = 0.1$.

5.1. The Hölder exponent α. In his study of the finite-time blow-up of the axisymmetric Euler equations with no swirl and with Hölder continuous initial data [15], Elgindi assumes that α is very close to zero, smaller than 10^{-14}. Such small value of α is used to control the higher order terms of α in Elgindi's proof. However, as stated in the Conjecture 8 of [13] by Drivas and Elgindi, such a blow-up may still hold for a range of $\alpha \in (0, 1/3)$ for the 3D Euler equations. For $\alpha > 1/3$, it has been shown by [47, 43, 44, 42, 11, 1] that the solution will be globally regular.

Therefore, we try different Hölder exponent α and explore the window of α that admits potential finite-time blow-up. For each α, we first use the adaptive mesh method to solve the equations (1.5) close enough to its potential blow-up time, and then use the dynamic rescaling method (4.1) to continue the computation and capture the self-similar profile.

For our 3D Euler equations with initial data (2.5) with $\alpha = 0.05, 0.10, 0.15, 0.20, 0.25, 0.30$, we obtain strong evidence for the formation of self-similar singularity. The steady states of the solutions are plotted in Figure 20. We can see that as α increases, $\tilde{\omega}_1$ will have weaker dependence on ξ, and the self-similar profile becomes more and more one-dimensional. We plot the cross sections of the steady states of $\tilde{\omega}_1$ in Figure 21. As α increases, $-\tilde{\omega}_1(\xi, 1)$ becomes more and more flat, especially in the local window around $\xi = 0$. Moreover, $-\tilde{\omega}_1(0, \zeta)$ seems to be insensitive to the value of α.

As α increases, c_l increases rapidly. We can see from Figure 22 that, c_l is more than 100 when $\alpha = 0.3$. Such large c_l can cause a lot of troubles for our adaptive mesh method, as the collapsing speed of the solution is extremely fast. Fortunately, the dynamic rescaling method is stable with large c_l, as the extra stretching term can control the rate of collapse. We list the values of c_l for different α in Table 3 in the next section.

For $\alpha > 0.30$, like $\alpha = 0.31, 0.40, 0.50$, we observe that although $\|\tilde{\omega}\|_{L^\infty}$ grows rapidly in the initial stage, it eventually slows down and starts to decrease, and the dynamic rescaling formulation fails to converge to a steady state. For example, in the case of $\alpha = 0.31$ shown in Figure 23, the double logarithm of $\|\omega\|_{L^\infty}$ becomes sublinear in the late stage, and $\|\omega\|_{L^\infty}^{-1}$ seems to decay slowly to zero, which would violate the Beale-Kato-Majda blow-up criterion. While the value $\alpha = 0.31$ is still far from the critical case of $\alpha = 1/3$, we remark that this is due to our choice of the physical domain and initial data. In the next section we explore a class of initial data that would enable us to push the blow-up parameter region for α much closer to the

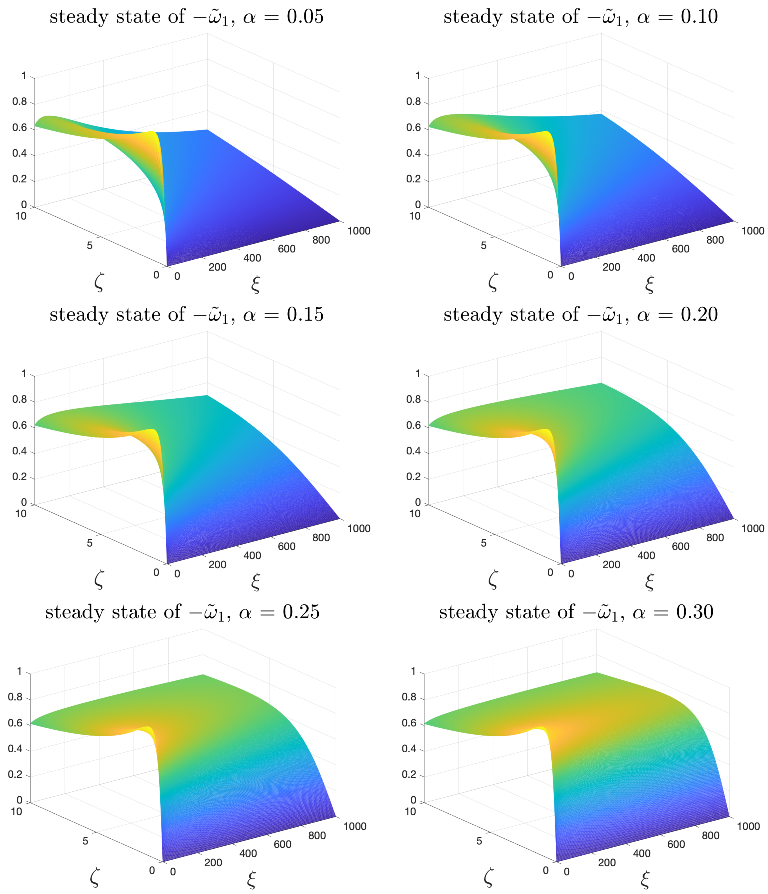

FIG. 20. *Steady states of* $-\tilde{\omega}_1$ *with different* α *in* $\mathbb{R}^3$.

critical value $\alpha = 1/3$.

5.2. The anisotropic scaling parameter δ. As the numerical results in Section 3.1 show, the initial data generate a hyperbolic flow around the origin as in Figure 4, where we observe a fast collapse of the solution along the z-direction. This strong collapsing force in z drives the solution to be singular in an extremely fast manner, which significantly limits our ability to push the computation sufficiently close to the potential singularity time. Therefore, we naturally ask if stretching the physical domain and the initial data in the z-direction would enhance the chance of producing a finite-time blow-up for a larger range of α.

We stretch the physical domain $(r,z) \in [0,1] \times \left[0, \frac{1}{2}\right]$ to $[0,1] \times \left[0, \frac{1}{2\delta}\right]$, and stretch the initial data $\omega_1^\circ(r,z)$ to $\omega_1^\circ(r,\delta z)$. Here δ is the parameter controlling the stretch or squeeze. The case of $\delta = 1$ corresponds to no stretch and $\delta < 1$, $\delta > 1$ correspond to stretch and squeeze, respectively. Instead of redefining the physical domain $\mathcal{D}$ and the initial data (2.5), we define the new variables

$$\hat{\omega}_1(r,z,t) = \omega_1(r,z/\delta,t/\delta), \quad \hat{\psi}_1(r,z,t) = \psi_1(r,z/\delta,t/\delta), \tag{5.1}$$

In the following, we will slightly abuse the notations by still using the symbol ω_1 and

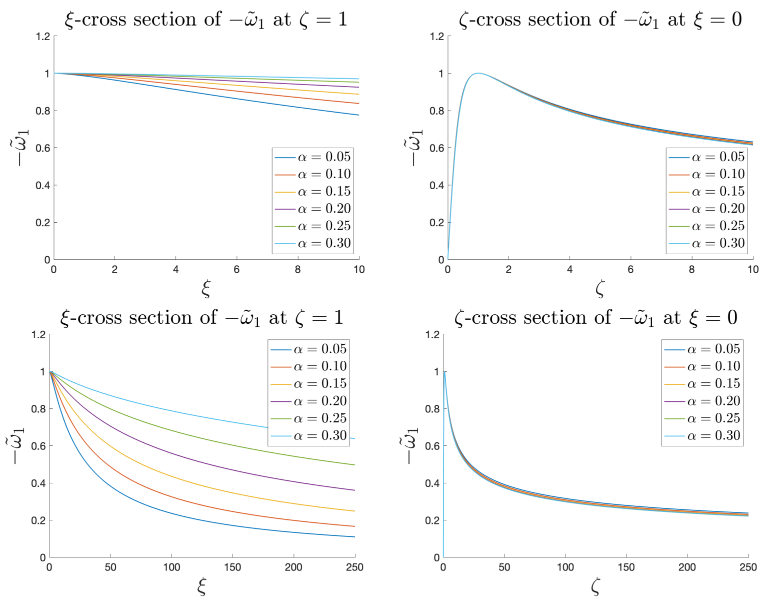

FIG. 21. *Cross sections of steady states of $-\tilde{\omega}_1$ with different α. Top row: on a local window. Bottom row: on a larger window.*

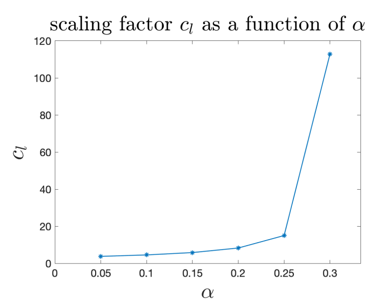

FIG. 22. *The scaling factor c_l as a function of α.*

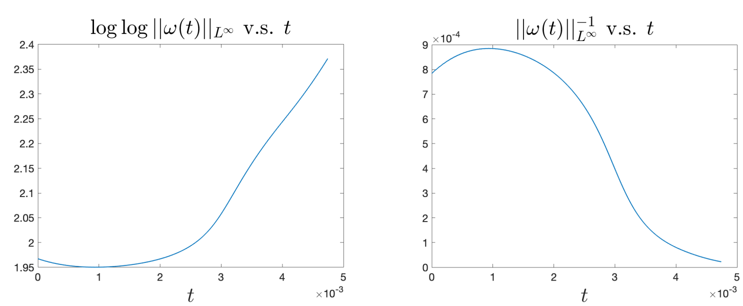

FIG. 23. *Evidence of no blow-up for $\alpha = 0.31$ in $\mathbb{R}^3$.*

ψ_1 to represent $\hat{\omega}_1$ and $\hat{\psi}_1$. With the newly defined variables, (1.5) becomes

$$\omega_{1,t} + u^r \omega_{1,r} + u^z \omega_{1,z} = -(1-\alpha)\psi_{1,z}\omega_1, \tag{1.5a'}$$

$$-\psi_{1,rr} - \delta^2 \psi_{1,zz} - \frac{3}{r}\psi_{1,r} = \omega_1 r^{\alpha-1}, \tag{1.5b'}$$

$$u^r = -r\psi_{1,z}, \quad u^z = 2\psi_1 + r\psi_{1,r}. \tag{1.5c'}$$

The physical domain $\mathcal{D}$ and the initial data (2.5) remain unchanged. The only difference in (1.5') is that the Poisson equation (1.5b') has an additional coefficient δ^2 in front of the z-derivative term $\psi_{1,zz}$. Similarly, the new dynamic rescaling formulation will be the same as (4.1), except that there is an extra coefficient δ^2 in front of $\tilde{\psi}_{1,\zeta\zeta}$ in the Poisson equation (4.1b).

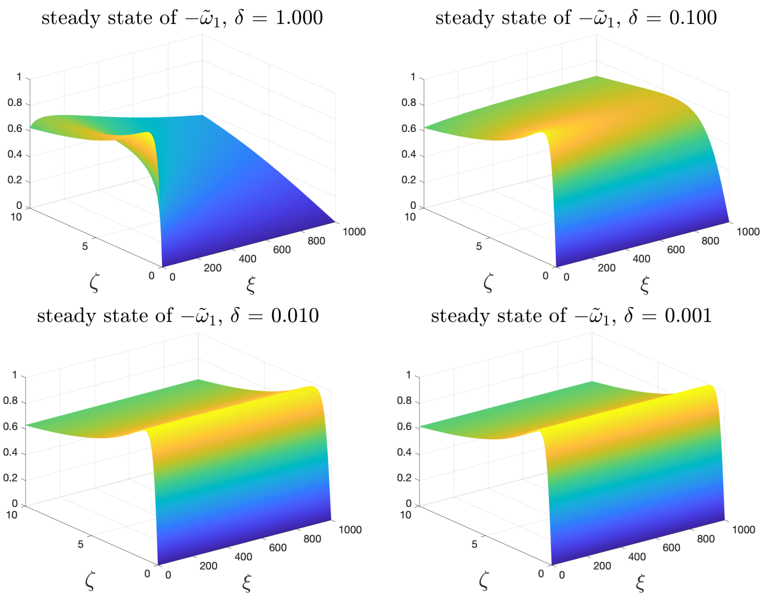

FIG. 24. *Steady states of $-\tilde{\omega}_1$ with different δ in $\mathbb{R}^3$ with $\alpha = 0.1$.*

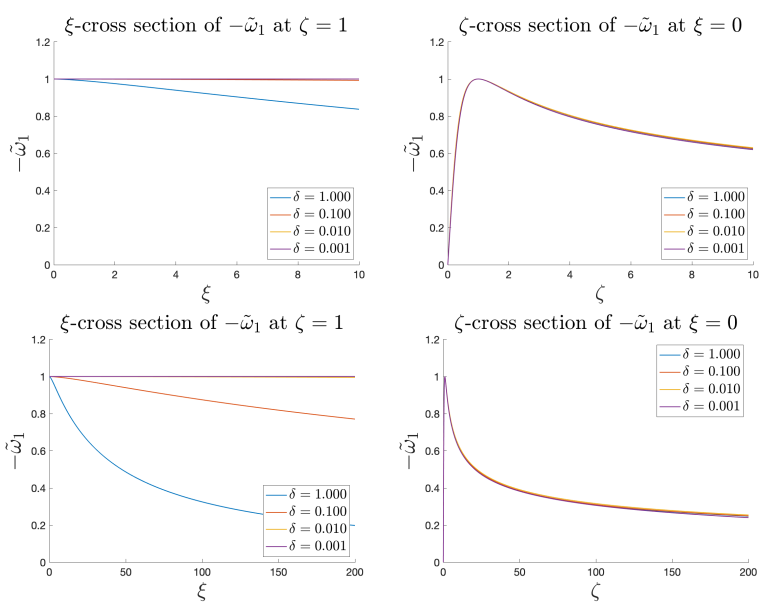

FIG. 25. *Cross sections of steady states of $-\tilde{\omega}_1$ with different δ with $\alpha = 0.1$. Top row: on a local window. Bottom row: on a larger window.*

We solve the equations (1.5') with different values of δ. In Figure 24, we plot the steady state profiles of $-\tilde{\omega}_1$ with different δ. In Figure 25, we plot the cross sections of the steady states of $-\tilde{\omega}_1$ with different δ. As δ decreases, the near field of the steady state profile tends to be closer to a 1D structure. The ξ-cross section of $-\tilde{\omega}_1$ at $\zeta = 1$ becomes remarkably flat for small values of δ. And it seems that the ζ-cross section of $-\tilde{\omega}_1$ at $\xi = 0$ is insensitive to the value of δ. We refer to [23] for more discussion on the limiting behavior of the steady state profile.

c_l		δ			
		10^0	10^{-1}	10^{-2}	10^{-3}
α	0.05	3.771	3.563	2.835	2.478
	0.10	4.549	4.242	3.377	2.995
	0.15	5.818	5.331	4.238	3.799
	0.20	8.270	7.373	5.797	5.219
	0.25	15.00	12.57	9.414	8.390
	0.30	112.8	51.68	26.57	21.68
	0.31	-	146.2	42.24	31.81
	0.32	-	-	103.7	59.76
	0.33	-	-	-	495.0

TABLE 3
The scaling factors c_l in $\mathbb{R}^3$ for different choices of α and δ.

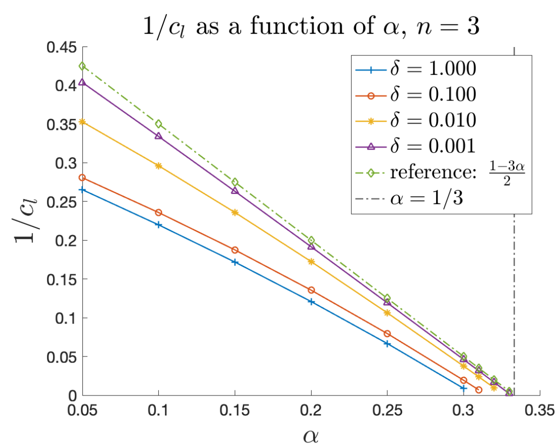

FIG. 26. *$1/c_l$ as a function of α.*

In Table 3, we list the converged values of c_l for different values of α and δ. Some cells are left empty because we do not observe a potential finite-time blow-up for that particular pair of parameters. We can clearly see that c_l monotonically increases with α and δ. When α is approaching the critical cut-off value between blow-up and no blow-up, c_l becomes extremely large.

In Figure 26, we plot $1/c_l$ versus α. We see that $1/c_l$ decreases with α and seems to converge to zero as α approaches $\alpha^* < 1/3$, which implies that $c_l \to \infty$. Such a limit corresponds to some limiting behavior of the 3D Euler equations. The critical α that makes c_l infinity is smaller than $1/3$, and increases as δ decreases to zero.

Figure 26 also implies that by simply stretching physical domain and initial data, controlled by the parameter δ, we can obtain a class of potential self-similar blow-up with a continuous range of scaling factor c_l. In other words, there are infinitely many possible scaling factors c_l for the potential self-similar blow-up of 3D axisymmetric Euler equations with no swirl.

The limiting case of $\delta \to 0$ seems to be most interesting. Here in Figure 26 we draw the line of $\frac{1-3\alpha}{2}$ in green and dash as a reference. Firstly, we observe that as δ decreases, the curve of $1/c_l$ becomes more linear with respect to α and gets closer to the reference line. Indeed, at $\delta = 10^{-3}$, regression shows that $1/c_l$ has an R^2 of more than $1 - 6.68 \times 10^{-5}$ with α. We would like to point out that this regression is done with only 9 data points listed in Table 3. But we believe this is a strong implication that $1/c_l$ is linear with α as $\delta \to 0$. We report the similar phenomenon for the n-D Euler equations in [23], where now the reference line has the form $\frac{n-2-n\alpha}{n-1}$.

Secondly, let us denote by α^* the critical value of α such that $1/c_l$ touches zero. Our numerical results seem to suggest that as $\delta \to 0$, α^* approaches $1/3$. If this is true, it will provide strong evidence supporting Conjecture 8 of [13] that the 3D Euler equations with C^α initial vorticity with $\alpha < 1/3$ would develop finite-time blow-up.

6. Sensitivity of the potential blow-up to initial data. We study the sensitivity of the potential self-similar blow-up to initial data. In addition to the initial data (2.5), we consider the following cases,

$$
\begin{aligned}
\omega_1^{\circ,1} &= -12000\left(1-r^2\right)^{18}\sin(2\pi z),\\
\omega_1^{\circ,2} &= -6000\cos\left(\frac{\pi r}{2}\right)\sin(2\pi z)\left(2+\exp\left(-r^2\sin^2(\pi z)\right)\right),\\
\omega_1^{\circ,3} &= \frac{-12000\left(1-r^2\right)^{18}\sin(2\pi z)^3}{1+12.5\sin^2(\pi z)}.
\end{aligned} \tag{6.1}
$$

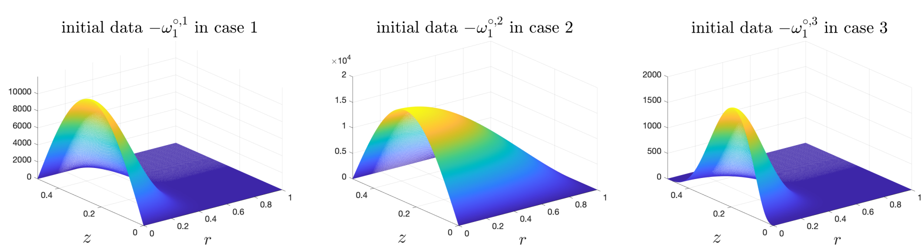

FIG. 27. *Profiles of the initial data in all three cases.*

We show the profiles of these three initial data in Figure 27. In Case 1, $\omega_1^{\circ,1}$ is a perturbation of ω_1° by setting the denominator to be 1. In Case 2, $\omega_1^{\circ,2}$ has a decay rate in r slower than $\left(1-r^2\right)^{18}$, and is no longer a tensor product of r and z. In Case 3, $\omega_1^{\circ,3}$ has an improved regularity in ρ near the origin. Indeed, we have, with $\omega_1(r,z,0) = \omega_1^{\circ,3}(r,z)$,

$$
\omega^\theta(r,z,0) = r^\alpha \omega_1^{\circ,3}(r,z) \sim r^\alpha z^3 = \rho^{3+\alpha}\cos^\alpha\theta\sin^3\theta.
$$

While for the original choice of the initial data (2.5), $\omega^\theta(r,z,0) \sim \rho^{1+\alpha}\cos^\alpha\theta\sin\theta$.

For all three cases, we only solve the 3D Euler equations with $\alpha = 0.3$ and $\delta = 1$, due to the limited computational resources. As shown in Table 3, for our original initial data, $c_l = 112.8$ is very large, which suggests that our choice of α and δ is very close to the borderline between the blow-up and non-blow-up. If the blow-up profile of the above initial data agrees with our original initial data well, we then have good confidence that they should have the same behavior for other settings of α and δ.

We solve the 3D Euler equations with the above initial data by first using the adaptive mesh method to get close enough to the potential blow-up time, and then using the dynamic rescaling method to capture the potential self-similar solution.

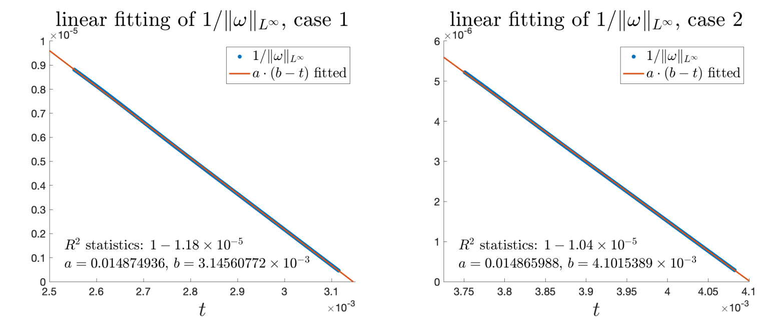

FIG. 28. *Fitting of $1/\|\omega\|_{L^\infty}$ with time t in the first and second cases.*

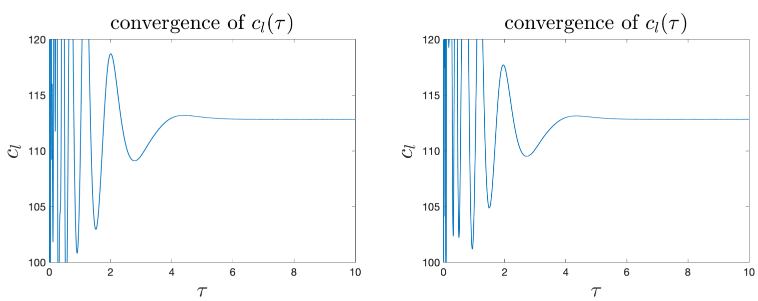

FIG. 29. *Curves of the scaling factor c_l in the first and second cases.*

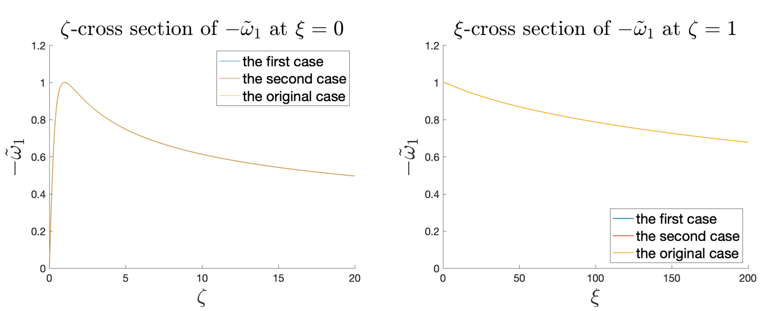

FIG. 30. *Cross sections of the steady states of $-\tilde{\omega}_1$ in the first and second cases.*

For the first and second cases, we show the fitting of $1/\|\omega\|_{L^\infty}$ with time t in Figure 28, and the curve of the scaling factor c_l in Figure 29. We can see that in both cases, $\|\omega\|_{L^\infty}$ scales like $1/(T-t)$, which implies a finite-time blow-up. Moreover, c_l converges to 112.8, matching the value of c_l we obtained using the original initial data well. In Figure 30, we show the cross sections of the steady state of $-\tilde{\omega}_1$ in comparison with the result obtained using the original initial data. There is no visible difference between the three steady states presented. In fact, even on the whole computational domain $\mathcal{D}' = \left\{(\xi,\zeta) : 0 \le \xi \le 1\times 10^5, 0 \le \zeta \le 5\times 10^4\right\}$ in the dynamic rescaling computation, the steady states in the first and second cases only differ by 7.03×10^{-10} and 5.29×10^{-10} respectively from the steady state using our original initial data ω_1° in the relative sup-norm.

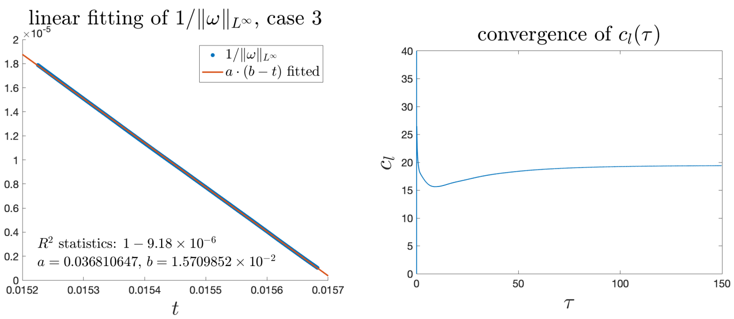

FIG. 31. *Fitting of* $1/\|\omega\|_{L^\infty}$ *and curve of the scaling factor* c_l *in the third case.*

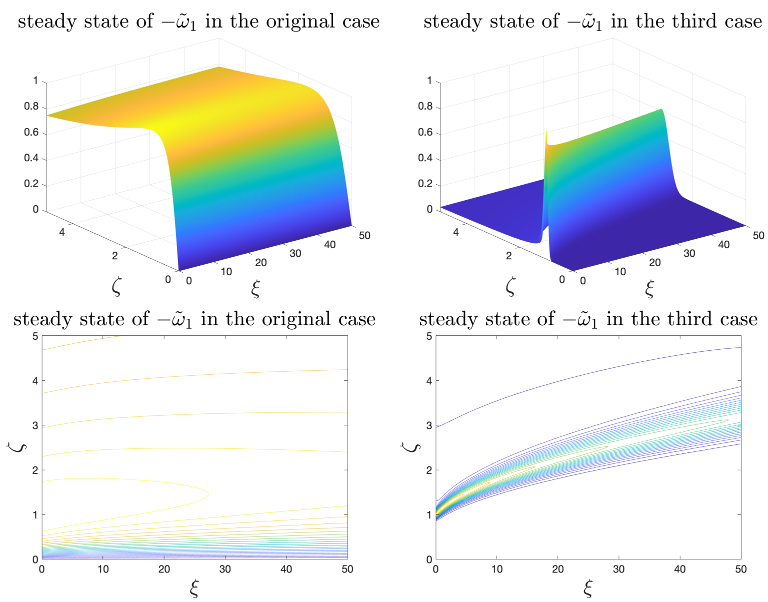

FIG. 32. *Profiles and contours of the steady states of* $-\tilde{\omega}_1$ *in the original and third cases.*

For the third case, the fitting of $1/\|\omega\|_{L^\infty}$ and the curve of the scaling factor c_l is shown in Figure 31. We observe that $1/\|\omega\|_{L^\infty}$ has a good linear fitting with time, suggesting a finite-time blow-up. However, c_l converges to 19.44 which is clearly different from 112.8, suggesting that there might be a new blow-up mechanism. In Figure 32, we compare the steady states of $\omega_1^{\circ,3}$ and ω_1° in the 3D profiles and the 2D contours. The steady state of $\omega_1^{\circ,3}$ has a slower change near $z=0$. This might be caused by the smoothness of the initial data near $z=0$. We have $\omega_1^{\circ,3} \sim r^\alpha z^3$, in contrast to $\omega_1^\circ \sim r^\alpha z$ near $(r,z)=(0,0)$. The steady state of the third case develops a channel-like structure that is not parallel to either axis.

The new blow-up scenario in the third case provides some support of Conjecture 9 of [13], in which the authors conjectured that the 3D Euler equations could still develop a finite-time blow-up for initial data that are C^∞ in ρ. In our future study, we plan to investigate the potential blow-up using a class of initial data of the form

$$\omega_1^{\circ,4} = -12000\left(1-r^2\right)^{18}\sin(2\pi z)^{2k+1},$$

with a positive integer k, so that $\omega_1^{\circ,4} \sim r^\alpha z^{2k+1} = \rho^{2k+1+\alpha}\cos^\alpha\theta\sin^{2k+1}\theta$ is C^{2k+1} in ρ.

7. Comparison with Eligindi's singularity. In this section, we compare our blow-up scenario with the scenario in [15] studied by Elgindi.

Elgindi introduced a polar coordinate system on the (r,z)-plane to construct his blow-up solution. More specifically, he introduced

$$\rho = \sqrt{r^2+z^2}, \quad \theta = \arctan\left(\frac{z}{r}\right).$$

Then for a Hölder exponent α, he introduced a change of variable $R=\rho^\alpha$ and define the variables

$$\Omega(R,\theta) = \omega^\theta(r,z), \quad \Psi(R,\theta) = \frac{1}{\rho^2}\psi^\theta(r,z).$$

In this setting, (1.3) can be rewritten as

(7.1a)

$$\Omega_t + (3\Psi + \alpha R\Psi_R)\,\Omega_\theta - (\Psi_\theta - \Psi\tan\theta)\,\Omega_R = (2\Psi\tan\theta + \alpha R\Psi_R\tan\theta + \Psi_\theta)\,\Omega,$$

(7.1b)

$$-\alpha^2R^2\Psi_{RR} - \alpha(5+\alpha)R\Psi_R - \Psi_{\theta\theta} + (\Psi\tan\theta)_\theta - 6\Psi = \Omega.$$

Elgindi's analysis of (7.1b) establishes the following leading order approximation for small α

$$\Psi(R,\theta) = \frac{1}{4\alpha}\sin(2\theta)L_{12}(\Omega)(R) + \text{lower order terms}, \tag{7.2}$$

where

$$L_{12}(\Omega)(R) = \int_R^\infty\int_0^{\frac{\pi}{2}} \Omega(s,\theta)\frac{K(\theta)}{s}\mathrm{d}s\mathrm{d}\theta,$$

with $K(\theta) = 3\sin\theta\cos^2\theta$. If we plug in the approximation (7.2) to (7.1a), neglecting lower order terms of α, and (time) scaling out some constant factor, we arrive at Elgindi's fundamental model

$$\Omega_t = \frac{1}{\alpha}L_{12}(\Omega)\Omega, \tag{7.3}$$

which admits self-similar finite-time blow-up. In his analysis, Elgindi chose the following self-similar solution of the fundamental model (7.3)

$$\Omega(R,\theta,t) = \frac{c}{1-t}F\left(\frac{R}{1-t}\right)\left(\sin\theta\cos^2\theta\right)^{\alpha/3}, \tag{7.4}$$

where $c > 0$ is some fixed constant, and $F(z) = 2z/(1+z)^2$.

One difference between our blow-up scenario and Engindi's blow-up scenario is how the scaling factor c_l depends on α. We rewrite (7.4) as

$$\Omega = \frac{c}{1-t} F\left(\frac{\rho^\alpha}{1-t}\right)\left(\frac{r^2 z}{\rho^3}\right)^{\alpha/3} = \frac{c}{1-t} F\left(\left(\frac{\rho}{(1-t)^{1/\alpha}}\right)^\alpha\right)\left(\frac{r^{2/3} z^{1/3}}{\rho}\right)^\alpha .$$

If we let $G(z) = F(z^\alpha)$, we see

$$\Omega = \frac{c}{1-t} G\left(\frac{\rho}{(1-t)^{1/\alpha}}\right)\left(\frac{r^{2/3} z^{1/3}}{\rho}\right)^\alpha .$$

Since $r^{2/3} z^{1/3}/\rho$ is homogeneous, we may conclude that the scaling factors for the self-similar blow-up solution (7.4) are

$$c_l = 1/\alpha, \quad c_\omega = 2.$$

Note that this also satisfies the relation $c_\omega = 1 + \alpha c_l$ in (2.8). This implies that c_l decreases as α increases, and c_l will tend to infinity as $\alpha \to 0$. However, as shown in Figure 26, our c_l increases as α increases, and $c_l \to +\infty$ when α tends to some α^* below $1/3$, and α^* is approaching $1/3$ as the parameter δ approaches zero.

Furthermore, the regularity of our initial data as a function of ρ is different from that of Elgindi's initial data. Around $(r, z) = (0, 0)$, Elgindi's initial condition has the following leading order behavior

$$\Omega \sim \rho^\alpha \left(\sin\theta \cos^2\theta\right)^{\alpha/3} = r^{2\alpha/3} z^{\alpha/3}.$$

However, our initial condition gives

$$\omega^\theta = r^\alpha \omega_1^\circ \sim r^\alpha z = \rho^{1+\alpha} \cos^\alpha\theta \sin\theta.$$

These two leading order scaling properties differ from each other in that

- Elgindi's initial condition of ω^θ has a C^α Hölder continuity in ρ, whereas ours is $C^{1,\alpha}$ in ρ,
- Elgindi's initial condition of ω^θ has a Hölder continuity near $z = 0$, whereas our initial condition is smooth in z.

In Conjecture 8 of [13], the authors conjectured that the initial data could be C^∞ in ρ for finite-time blow-up of the 3D axisymmetric Euler equations with no swirl. Our initial data slightly improves the regularity of the initial data in ρ. In [48], the second author has also explored the initial data with higher regularity in ρ.

In Lemma 4.33 of [13], the authors stated that the limiting equations at $\alpha = 0$ of (7.1), can blow up in finite time for initial data of Ω that only has a C^α-Hölder continuity near $r = 0$ for $\alpha < 1/3$. Our study shows that the blow-up of the axisymmetric Euler equations does not require to have Hölder continuity of the initial vorticity along the z-direction. The essential driving force for the finite-time blow-up comes from the Hölder continuity of the initial vorticity along the r-direction.

8. Concluding remarks. In this paper, we have numerically studied the singularity formation in the axisymmetric Euler equations with no swirl when the initial condition for the angular vorticity is C^α Hölder continuous. With carefully-chosen initial data and specially-designed adaptive mesh, we have solved the solution very close to the potential blow-up time, and obtained strong convincing numerical evidence for the singularity formation by numerically examining the Beale-Kato-Majda blow-up criterion. Scaling analysis and dynamic rescaling method have further suggested the potential self-similar blow-up. By introducing an isotropic scaling parameter δ that stretches the initial data and the Euler equations along the z-axis, we observed the potential self-similar blow-up in finite time when the Hölder exponent α is smaller than some α^*, and this upper bound α^* can asymptotically approach $1/3$ as δ goes to 0. Since when $\alpha > 1/3$, the axisymmetric Euler equations with no swirl admit global regularity [47, 43, 44, 42, 11, 1], this would potentially close gap between blow-up and non-blow-up, leaving only the critical case of $\alpha = 1/3$.

The potential blow-up observed in this paper is insensitive to the perturbation of initial data. And our initial study suggested that the regularity of the initial data around the origin would determine its scaling properties and the shape of the self-similar blow-up profile. Compared with Elgindi's blow-up result reported in [15], our potential blow-up scenario has very different scaling properties. The regularity properties of the initial condition of the two initial data are also quite different.

In our subsequent paper [23], we will further explore the potential singularity formation in the high-dimensional case of the Euler equations. We demonstrate that our settings of the boundary condition and initial data would consistently lead to potential singularity formation in high space dimensions. Moreover, we propose a possible mechanism, which implies the 3D axisymmetric Euler equations with no swirl would develop finite-time blow-up for a range for the Hölder exponent α. Surprisingly, this range of α matches well with our numerical results in different dimensions. We also propose a relatively simple 1D model and demonstrate that this one-dimensional model provides a very good approximation to the 3D Euler equations. This 1D model could play a role similar to the leading order system derived by Elgindi in [15] in the analysis of the finite time singularity of the 3D Euler equations.

Acknowledgments. The research was in part supported by DMS-2205590. We would like to acknowledge the generous support from Mr. K. C. Choi through the Choi Family Gift Fund and the Choi Family Postdoc Gift Fund.

REFERENCES

[1] H. Abidi, T. Hmidi, and S. Keraani, *On the global well-posedness for the axisymmetric Euler equations*, Mathematische Annalen, 347 (2010), pp. 15–41.

[2] J. T. Beale, T. Kato, and A. Majda, *Remarks on the breakdown of smooth solutions for the 3D Euler equations*, Communications in Mathematical Physics, 94 (1984), pp. 61–66.

[3] M. D. Bustamante and R. M. Kerr, *3D Euler about a 2D symmetry plane*, Physica D: Nonlinear Phenomena, 237 (2008), pp. 1912–1920.

[4] R. E. Caflisch, *Singularity formation for complex solutions of the 3D incompressible Euler equations*, Physica D: Nonlinear Phenomena, 67 (1993), pp. 1–18.

[5] J. Chen and T. Y. Hou, *Finite time blowup of 2D Boussinesq and 3D Euler equations with $C^{1,\alpha}$ velocity and boundary*, Communications in Mathematical Physics, 383 (2021), pp. 1559–1667.

[6] J. Chen and T. Y. Hou, *Stable nearly self-similar blowup of the 2D Boussinesq and 3D Euler equations with smooth data*, arXiv preprint arXiv:2210.07191, (2022).

[7] J. Chen, T. Y. Hou, and D. Huang, *Asymptotically self-similar blowup of the Hou-Luo model for the 3D Euler equations*, arXiv preprint arXiv:2106.05422, (2021).

[8] J. Chen, T. Y. Hou, and D. Huang, *On the finite time blowup of the De Gregorio model for the 3D Euler equations*, Communications on pure and applied mathematics, 74 (2021), pp. 1282–1350.

[9] K. Choi, T. Y. Hou, A. Kiselev, G. Luo, V. Sverak, and Y. Yao, *On the finite-time blowup of a one-dimensional model for the three-dimensional axisymmetric Euler equations*, Com-

munications on Pure and Applied Mathematics, 70 (2017), pp. 2218–2243.
[10] P. Constantin, C. Fefferman, and A. J. Majda, *Geometric constraints on potentially singular solutions for the 3D Euler equations*, Communications in Partial Differential Equations, 21 (1996).
[11] R. Danchin, *Axisymmetric incompressible flows with bounded vorticity*, Russian Mathematical Surveys, 62 (2007), p. 475.
[12] J. Deng, T. Y. Hou, and X. Yu, *Geometric properties and nonblowup of 3D incompressible Euler flow*, Communications in Partial Difference Equations, 30 (2005), pp. 225–243.
[13] T. D. Drivas and T. M. Elgindi, *Singularity formation in the incompressible Euler equation in finite and infinite time*, arXiv preprint arXiv:2203.17221, (2022).
[14] W. E and C.-W. Shu, *Numerical study of the small scale structures in Boussinesq convection*, tech. report, 1992.
[15] T. M. Elgindi, *Finite-time singularity formation for $C^{1,\alpha}$ solutions to the incompressible Euler equations on $\mathbb{R}^3$*, Annals of Mathematics, 194 (2021), pp. 647–727.
[16] C. L. Fefferman, *Existence and smoothness of the Navier-Stokes equation*, The millennium prize problems, 57 (2000), p. 67.
[17] A. B. Ferrari, *On the blow-up of solutions of the 3D Euler equations in a bounded domain*, Communications in mathematical physics, 155 (1993), pp. 277–294.
[18] J. D. Gibbon, *The three-dimensional Euler equations: Where do we stand?*, Physica D: Nonlinear Phenomena, 237 (2008), pp. 1894–1904.
[19] R. Grauer and T. C. Sideris, *Numerical computation of 3D incompressible ideal fluids with swirl*, Physical review letters, 67 (1991), p. 3511.
[20] T. Y. Hou, *The nearly singular behavior of the 3D Navier-Stokes equations*, arXiv preprint arXiv:2107.06509, (2021).
[21] T. Y. Hou, T. Jin, and P. Liu, *Potential singularity for a family of models of the axisymmetric incompressible flow*, Journal of Nonlinear Science, 28 (2018), pp. 2217–2247.
[22] T. Y. Hou and R. Li, *Dynamic depletion of vortex stretching and non-blowup of the 3D incompressible Euler equations*, Journal of Nonlinear Science, 16 (2006), pp. 639–664.
[23] T. Y. Hou and S. Zhang, *Potential singularity of the axisymmetric Euler equations with C^α initial vorticity for a large range of α. Part II: n-dimensional case*, arXiv preprint arXiv:2212.xxxxx, (2022).
[24] R. M. Kerr, *Evidence for a singularity of the three-dimensional, incompressible Euler equations*, Physics of Fluids A: Fluid Dynamics, 5 (1993), pp. 1725–1746.
[25] R. M. Kerr, *Bounds for Euler from vorticity moments and line divergence*, Journal of Fluid Mechanics, 729 (2013).
[26] A. Kiselev, *Small scales and singularity formation in fluid dynamics*, in Proceedings of the International Congress of Mathematicians (ICM 2018) (In 4 Volumes) Proceedings of the International Congress of Mathematicians 2018, World Scientific, 2018, pp. 2363–2390.
[27] A. Kiselev, L. Ryzhik, Y. Yao, and A. Zlatoš, *Finite time singularity for the modified SQG patch equation*, Annals of mathematics, (2016), pp. 909–948.
[28] A. Kiselev and V. Šverák, *Small scale creation for solutions of the incompressible two-dimensional Euler equation*, Annals of mathematics, 180 (2014), pp. 1205–1220.
[29] M. Landman, G. Papanicolaou, C. Sulem, P. L. Sulem, and X. P. Wang, *Stability of isotropic self-similar dynamics for scalar-wave collapse*, Physical Review A, 46 (1992), p. 7869.
[30] M. J. Landman, G. C. Papanicolaou, C. Sulem, and P.-L. Sulem, *Rate of blowup for solutions of the nonlinear Schrödinger equation at critical dimension*, Physical Review A, 38 (1988), p. 3837.
[31] B. LeMesurier, G. Papanicolaou, C. Sulem, and P. Sulem, *Focusing and multi-focusing solutions of the nonlinear Schrödinger equation*, Physica D: Nonlinear Phenomena, 31 (1988), pp. 78–102.
[32] J.-G. Liu and W.-C. Wang, *Convergence analysis of the energy and helicity preserving scheme for axisymmetric flows*, SIAM journal on numerical analysis, 44 (2006), pp. 2456–2480.
[33] J.-G. Liu and W.-C. Wang, *Characterization and regularity for axisymmetric solenoidal vector fields with application to Navier–Stokes equation*, SIAM Journal on Mathematical Analysis, 41 (2009), pp. 1825–1850.
[34] P. Liu, *Spatial Profiles in the Singular Solutions of the 3D Euler Equations and Simplified Models*, PhD thesis, California Institute of Technology, 2017.
[35] G. Luo and T. Y. Hou, *Potentially singular solutions of the 3D axisymmetric Euler equations*, Proceedings of the National Academy of Sciences, 111 (2014), pp. 12968–12973.
[36] G. Luo and T. Y. Hou, *Toward the finite-time blowup of the 3D axisymmetric Euler equations: a numerical investigation*, Multiscale Modeling & Simulation, 12 (2014), pp. 1722–1776.

[37] G. Luo and T. Y. Hou, *Formation of finite-time singularities in the 3D axisymmetric Euler equations: a numerics guided study*, SIAM Review, 61 (2019), pp. 793–835.
[38] A. Majda and A. Bertozzi, *Vorticity and incompressible flow*, vol. 27, Cambridge University Press, 2002.
[39] D. W. McLaughlin, G. C. Papanicolaou, C. Sulem, and P.-L. Sulem, *Focusing singularity of the cubic Schrödinger equation*, Physical Review A, 34 (1986), p. 1200.
[40] G. Papanicolaou, C. Sulem, P. L. Sulem, and X. P. Wang, *The focusing singularity of the davey-stewartson equations for gravity-capillary surface waves*, Physica D: Nonlinear Phenomena, 72 (1994), pp. 61–86.
[41] A. Pumir and E. D. Siggia, *Development of singular solutions to the axisymmetric Euler equations*, Physics of Fluids A: Fluid Dynamics, 4 (1992), pp. 1472–1491.
[42] X. Saint Raymond, *Remarks on axisymmetric solutions of the incompressible Euler system*, Communications in partial differential equations, 19 (1994), pp. 321–334.
[43] P. Serfati, *Régularité stratifiée et équation d'Euler 3Da temps grand*, CR Acad. Sci. Paris Sér. I Math, 318 (1994), pp. 925–928.
[44] T. Shirota and T. Yanagisawa, *Note on global existence for axially symmetric solutions of the Euler system*, Proceedings of the Japan Academy, Series A, Mathematical Sciences, 70 (1994), pp. 299–304.
[45] M. Siegel and R. Caflisch, *Calculation of complex singular solutions to the 3D incompressible Euler equations*, Physica D: Nonlinear Phenomena, 238 (2009), pp. 2368–2379.
[46] G. Strang, *On the construction and comparison of difference schemes*, SIAM journal on numerical analysis, 5 (1968), pp. 506–517.
[47] M. Ukhovskii and V. Iudovich, *Axially symmetric flows of ideal and viscous fluids filling the whole space: Pmm vol. 32, no. 1, 1968, pp. 59–69*, Journal of applied mathematics and mechanics, 32 (1968), pp. 52–62.
[48] S. Zhang, *Singularity Formation in the High-Dimensional Euler Equations and Sampling of High-Dimensional Distributions by Deep Generative Networks*, PhD thesis, California Institute of Technology, 2023.